Chapter 4
Constant Flow Injection

4.1 Introduction

The hydro-mechanical coupling is one of the research hotspots in the fields of petroleum, mining and tunneling engineering. The hydro-mechanical coupling issues encountered in hydraulic fracturing process can be mainly reflected in two aspects: (1) shales are fractured by the constant flow. The breakdown of rock in this process is mainly manifested as instantaneous breakdown. The time to breakdown is usually less than 30 s [1]. (2) When constant high fluid pressure is applied for a long duration, the microcracks in the sample grow in a subcritical way. The macroscopic evolution of a hydraulic fracture is time-dependent, which is named "delayed initiation" [2]. In terms of the fluid pressure distribution in the fracture, the fluid pressure in the two hydraulic fracturing processes corresponds to the "non-uniform" and "constant" states, respectively. Different injection conditions cause the rock to deform and fracture in different mechanisms. The effects of fluid pressure on stress state, fracture propagation, and softening of rock matrix also differ significantly.

In the process of engineering practice, conventional hydraulic fracturing construction still prefers constant flow conditions (fracturing at a constant injection rate). The continuous increase of fluid pressure induces the instantaneous breakdown of rock, which promotes the intersection of hydraulic fractures with discontinuities (such as natural fractures, and beddings) to form a complex fracture network, thus creating a flow channel for subsequent alkane and thermal energy exploitation. Although many works have been focused on hydraulic fracture propagation under constant flow injection conditions, few efforts have paid attention to the microcrack evolution (acoustic emission events) before the breakdown occurs. In the following part, we will fracture shale with constant flow mode in the laboratory and investigate the fracture propagation under different axial stresses and injection rates.

Y. Zhao et al., *Hydraulic Fracturing and Rock Mechanics*,
https://doi.org/10.1007/978-981-99-2540-7_4

4.2 Instantaneous Fracturing Mechanism of Constant Flow Pressurization

Under the constant flow injection mode, before the hydraulic fracture starts to initiate, its length is 0, and the fluid pressure in the wellbore is constant at a certain time, as shown in Fig. 4.1(i) (the darker the color of the mineral, the greater its rigidity is). The fluid pressure in the wellbore gradually increases with time increases. The high-pressure fluid induces a high-stress area around the wellbore. The mineral particles near the wellbore have different deformation due to their different stiffness, which forms stress concentration in local areas, resulting in the primary weak surface cracking and generating hydraulic fractures, as shown in Fig. 4.1(ii) [3]. The high-pressure fluid accumulated in the wellbore immediately diffuses into the fracture to drive the hydraulic fracture's further propagation, causing the sample's instantaneous breakdown. In this process, due to the fluid flow in the main fracture, the fluid pressure presents a gradient distribution of non-uniform pressure from the injection point to the fracture tip [4]. Since the pump pressure curve and fracture morphology characteristics of shale constant flow hydraulic fracturing under a uniaxial stress state have been described in detail in Chap. 3, this section will focus on the analysis of the disturbance effect of axial stress (5, 15 and 25 MPa) and injection rate (3, 6, 12, 18 and 30 mL/min) on the shale instantaneous fracturing process.

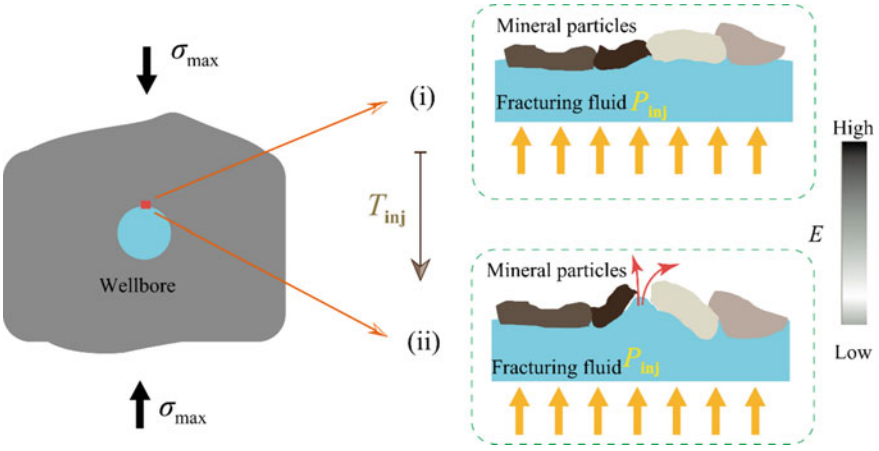

Fig. 4.1 Schematic of hydraulic fracture initiation around the wellbore under the constant flow injection condition

4.2.1 Impact of Axial Load

Under the uniaxial stress state, the axial stress is taken as the maximum principal stress (σ_{max}) that acts on the sample, so the disturbance of external stress to the hydraulic fracture is mainly reflected by the axial stress. According to the test scheme in Sect. 3.4.2 of Chap. 3 the sample is limited by axial stress in the whole hydraulic fracturing test process, including the preloading and hydraulic pressurization stages. Therefore, the disturbance effect of axial stress in the two stages is analyzed.

① **Preloading stage**

Referring to the experimental scheme of Lin et al. [5], the axial stress is preset as 5, 15 and 25 MPa. The axial stress, strain and AE characteristics during preloading are shown in Fig. 4.2. The axial loading rate is 0.5 MPa/min. With time elapsing, the axial strain (ε_a), circumferential strain (ε_h) and AE cumulative counts (AC) show a non-linear increasing trend, while the AE count rate presents an obvious segmentation characteristic. Combined with the axial stress variation, the preloading process can be further divided into two stages: (a) the micropore and fissure compaction stage; (b) the damage stable accumulation stage. The stage ① in Fig. 4.2a–c corresponds to the pores and fissures compaction stage. Under the initial axial load, the pores and fissures in the sample are closed or partially opened, resulting in the increase of axial and circumferential strains (in magnitude). Specifically, the sample is compacted in the axial direction and slightly expanded in the circumferential direction. Rapid closing or opening of micro pores and fissures will generate intense AE activities. According to Jiang et al. [6], the AE cumulative counts reflect the degree of damage in the rock. Therefore, the rapidly increasing AE cumulative counts imply the state of rapid accumulation of damage during the compaction stage. The stage ② in Fig. 4.2a–c corresponds to damage stable accumulation in the linear loading stage. With increasing axial strain, the circumferential strain increases continuously, which suggests that the sample still is in the radial expansion state in the linear elastic stage. Then, the AE cumulative counts began to increase progressively and steadily, indicating that the internal damage of the sample also cumulates correspondingly in the elastic loading stage. It is worth noting that even at the damage stable accumulation stage, the AE count rate still varies unstably with sudden jumps. This phenomenon may be explained by the growth of microcracks induced by the accumulation and/or release of the strain energy in the sample.

Figure 4.2d shows the relative changes of the axial strain, circumferential strain and AE cumulative counts in the compaction stage and the damage stable accumulation stage subject to different axial stresses. Overall, the axial strain in the compaction stage is greater than that in the damage stable accumulation stage. By comparison, the circumferential strain and AE cumulative counts are more likely to be affected by the axial stress. When the axial stress is relatively low (<5 MPa), the circumferential strain and AE activities are concentrated in the compaction stage. With the increase of the axial stress, the circumferential propagation deformation and AE cumulative counts in the linear elastic stage start to increase, indicating that higher axial stress can induce more damage in the sample.

The rock fracture process is often accompanied by unstable emission of AE signals [7, 8]. One single AE signal can be detected by multiple probes and output in the form of elastic waves of different frequency bands. Numerous studies have proven that [9–11], AE waveform signals contain information that can reflect the properties of AE sources, such as failure mode, crack coalescence pattern, and spatial scale of fractures. To reveal the microfracture mechanism of samples under different axial stress, this section will further carry out statistical analysis on the dominant frequency characteristics of AE waveforms. As shown in Fig. 4.3, the

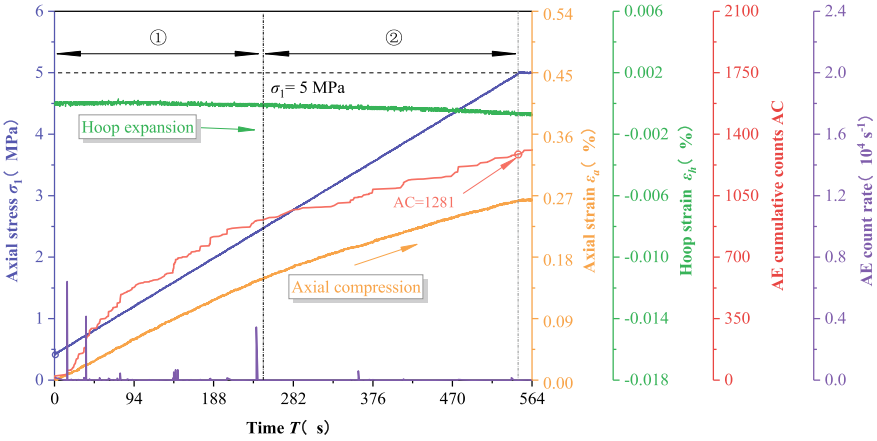

(a) Axial stress 5 MPa (Sample CA-90-5)

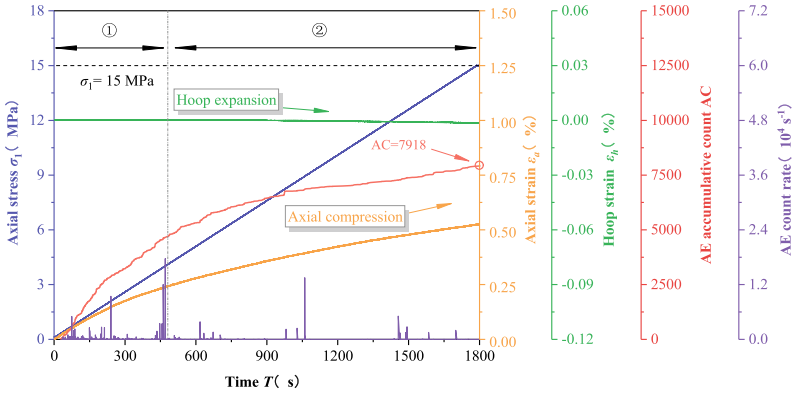

(b) Axial stress 15 MPa (Sample CA-90-15)

Fig. 4.2 Characteristics of sample deformation and AE during the preloading stage

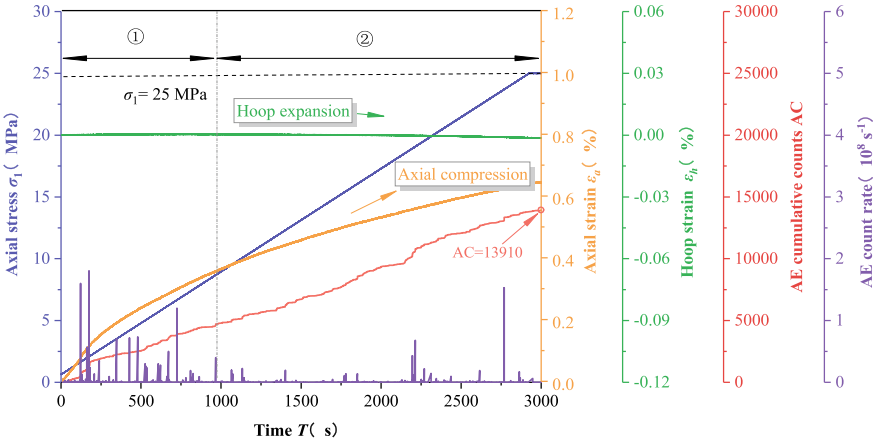

(c) Axial stress 25 MPa (Sample CA-90-25)

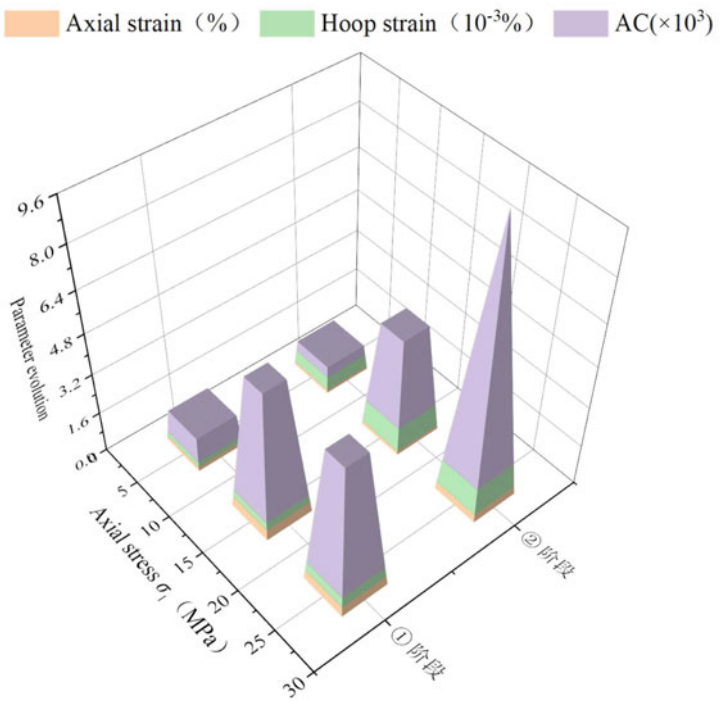

(d) Relative variation of deformation and AE parameters in different stages

Fig. 4.2 (continued)

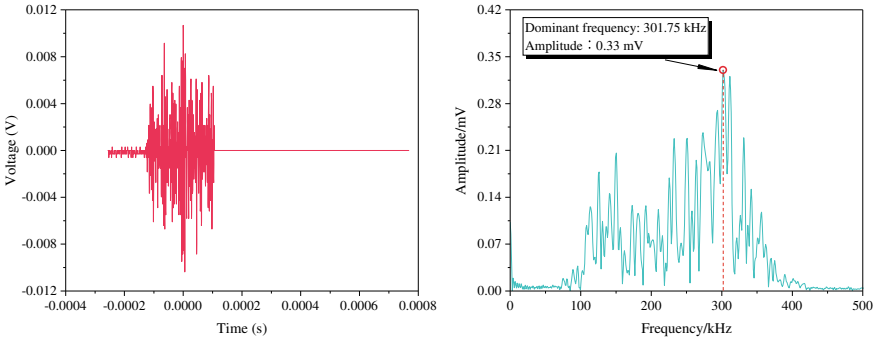

Fig. 4.3 An example of the dominant frequency extraction process

discrete time-domain waveform signals are transformed into continuous frequency-domain waveform signals utilizing the fast Fourier transform (FFT). The frequency corresponding to the maximum amplitude in the frequency domain spectrum is the dominant frequency of the AE waveform signal. Based on this principle, the time-varying dominant frequency characteristics of AE during preloading are explored by processing with MATLAB software and extracting the dominant frequency.

The mesoscopic fracture process of rock is characterized by different frequency response characteristics [12–14]. A lot of research has been carried out on the fracturing mechanism of rock using the first motion polarity method and moment tensor method, which reported that the rock fracture process presents obvious characteristics of two dominant frequency bands. Specifically, the tensile fracture in the rock generates the waveform signals with a low dominant frequency band, while the shear fracture produces a high dominant frequency band. However, the division of the dominant frequency band of AE has not formed a unified standard. Referring to the research ideas of Lei et al. [15], the AE signal during preloading is divided into three dominant frequency bands, namely, the low frequency band (0 ~ 140 kHz), medium frequency band (140 ~ 210 kHz) and high frequency band (210 ~ 350 kHz). Considering interference of the environmental noise, the actual value range of the low frequency band starts from 20 to 140 kHz. According to the frequency band characteristics of AE signals, the types of microcracks are classified, and the micro fracturing mechanism of rock during preloading is analyzed.

The time-varying evolution characteristics of AE signals in the frequency domain under different preload disturbances are shown in Fig. 4.4. It can be seen that the AE signal presents obvious dual dominant frequency band (high-low) characteristics. In addition, AE signals with low dominant frequency and low amplitude are mainly generated during the preloading process, which accounts for over 85%, indicating that the tensile fractures are mainly generated at the initial preloading stage. The medium dominant frequency signal appears in all axial loading processes, indicating that the mixed tensile-shear fractures occur in both of the compaction and the linear loading stages. In contrast, the high dominant frequency signal is more sensitive to the magnitude of the axial load. With the increase of axial load, the high frequency

signal in the sample begins to increase, implying that the increase of axial load will also induce more shear fractures.

① **Fluid injection process**

Figure 4.5 is the evolution curves of deformation, pump pressure and AE signal induced by fluid injection under different stress conditions. The hydraulic fracturing curves under constant injection rate ($Q_{inj} = 12$ mL/min) condition show the morphological characteristics of instantaneous change. At the initial pressurization stage (0 ~ 13 s), the sample's strain and AE signal change slightly. With the increase of pump pressure, the AE signal increases gradually accompanied by the axial and circumferential strains. When the pump pressure exceeds 80% of the breakdown pressure (P_b), the AE signal surges and the sample is hydraulically fractured followed by the subsequent sudden change of axial and circumferential deformation and steep drop of pump pressure. Afterward, the pump pressure declines to zero, the AE signal falls synchronously, and the axial and circumferential strains remain at an approximately constant level.

Under different axial stress conditions, the evolution of deformation and AE induced by fluid injection is also different. Comparing Fig. 4.5a–c, it can be found that when the initial axial stress is low ($\leq$5 MPa), the AE ring counting rate with an increasing rate from slow to fast will be generated in the pressurization and energy storage stage before fracturing. This indicates that the closing, initiation or reconnection of micro-cracks becomes more frequent, promoting the nonlinear increase of circumferential strain (Fig. 4.5a). With the increase of the initial axial stress, the axial restraint on the sample increases. Compared with the axial stress of 5 MPa, when the axial stress is 15 MPa, the activity and spanning time of AE before breakdown are significantly reduced, indicating that the micro-cracks in the sample are in a slow growth state where the cracks are instantaneously initiated or closed, which leads to a stepwise increase in the circumferential strain (Fig. 4.5b). When the axial stress is further increased to 25 MPa, it can be seen from Fig. 4.5c that there is almost no AE counting signals before the hydraulic breakdown, implying that the hydraulic fracturing process is featured by instantaneous breakdown under high-stress conditions. The circumferential strain is positive and increases gradually, indicating that the sample has a certain degree of shrinkage deformation in the radial direction during the injection process. This implies that the continuously increasing pump pressure under high axial stress (25 MPa) induces the opposite effect of the axial stress (compression and expansion). At lower axial stress, the pumping injection causes lateral expansion of the sample ($\varepsilon_h < 0$), which is beneficial to the axial compression and expansion. Under low axial stress (5 MPa and 15 MPa), the axial strain remains approximately constant. On the other hand, under the axial stress of 25 MPa, the axial strain shows a slowly increasing trend, indicating that under the action of high axial stress, the hydraulic pressurization causes the compressive deformation of the sample in the axial direction. These phenomena may be because the low axial stress is not enough to close the micro defects completely, so the pump pressure facilitates the main fractures to develop or close, thus contributing to the radial expansion of the sample. However, under high axial stress, the sample is in a

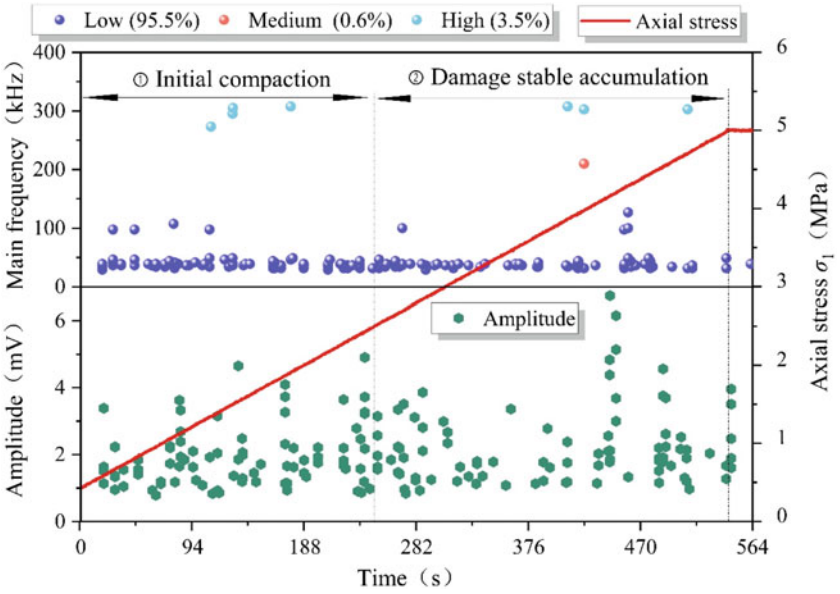

(a) Axial stress of 5 MPa (Sample CA-90-5)

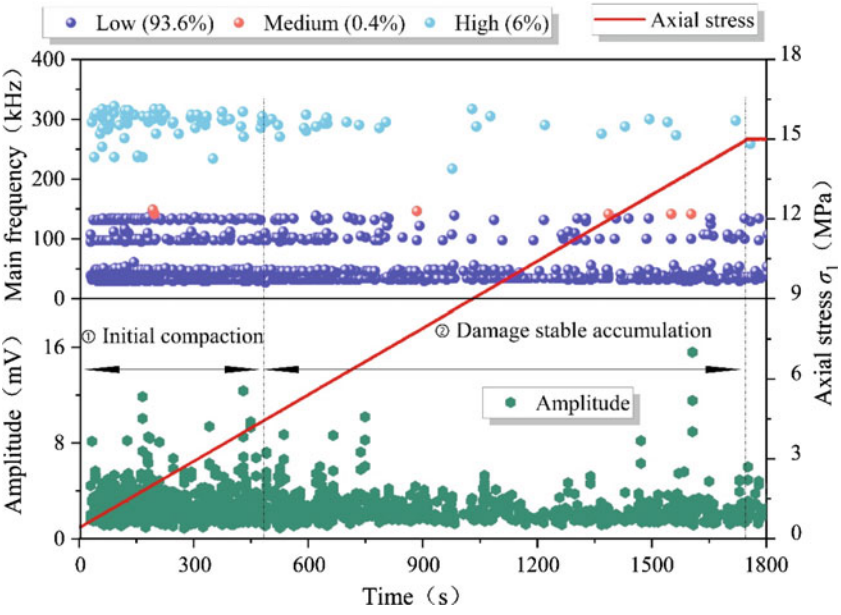

(b) Axial stress of 15 MPa (Sample CA-90-15)

Fig. 4.4 The time-varying characteristics of AE frequency domain during preloading process

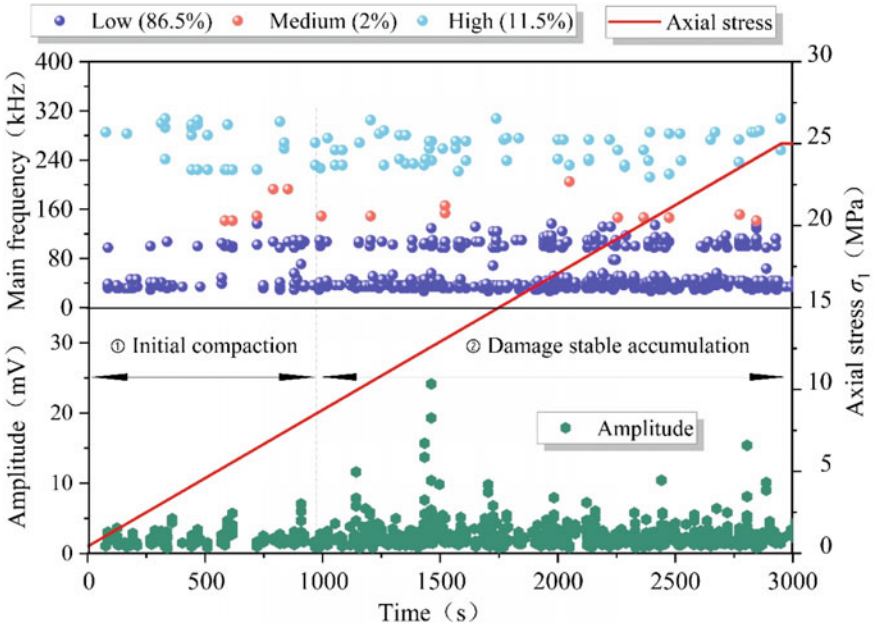

(c) Axial stress of 25 MPa (Sample CA-90-25)

Fig. 4.4 (continued)

completely compact state, and the pump pressure enlarges the pore pressure around the wellbore, resulting in shrinkage in both radial and axial directions.

Table 4.1 shows the comparison of breakdown pressure, instantaneous strain increment and AE signal characteristic parameters during hydraulic fracturing under different axial stresses. Where AC represents an AE cumulative (ringing) count, $\Delta\varepsilon_h$ and $\Delta\varepsilon_a$ is the circumferential and axial instantaneous strain increment, respectively. It can be seen from Table 4.1 that the breakdown pressure of rock decreases with the increase of Axial stress. The initial damage in the sample before the injection is small (Fig. 4.4), and the axial limit of the sample is small under the condition of low Axial stress. In the process of hydraulic injection, the micro-cracks close, crack and connect frequently. The energy accumulated by hydraulic pressurization can be released to a certain extent by opening or closing these defects, so higher pump pressure is required to crack the rock. On the contrary, compared with the low Axial stress, the samples with high Axial stress have more initial damage, and the pressure drop and energy consumed by the closure and communication of micro-fractures are small, which makes it possible to maintain effective pump pressure in the borehole and facilitate the induction of hydraulic fracturing under low pump pressure. In terms of rock deformation, with the increase of initial Axial stress, the instantaneous increment of circumferential strain increases gradually while the instantaneous increment of axial strain decreases gradually. It is shown that different axial stresses also have

different degrees of restraint (or promotion) on the deformation of the samples at the moment of fracturing, mainly showing that increasing the initial axial stress will promote radial expansion and inhibit axial compression. In addition, the cumulative counts and peak count rate of AE are negatively correlated with the change of axial

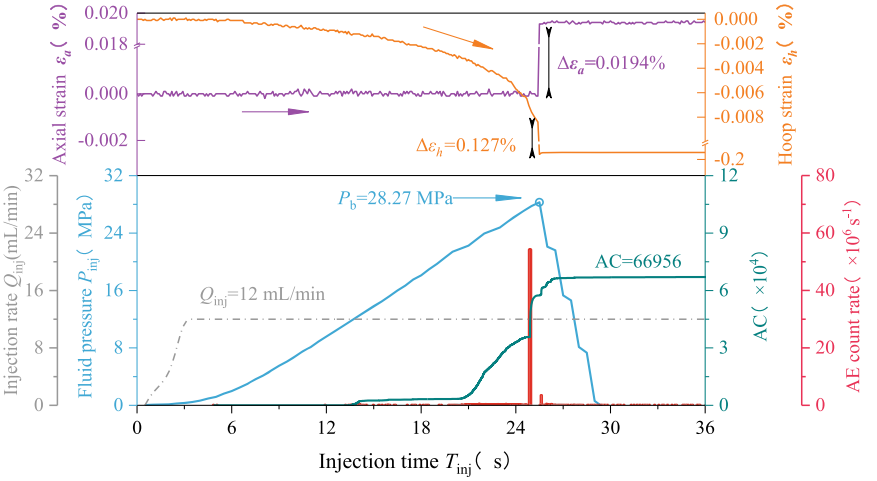

(a) Axial stress of 5 MPa (Sample CA-90-5)

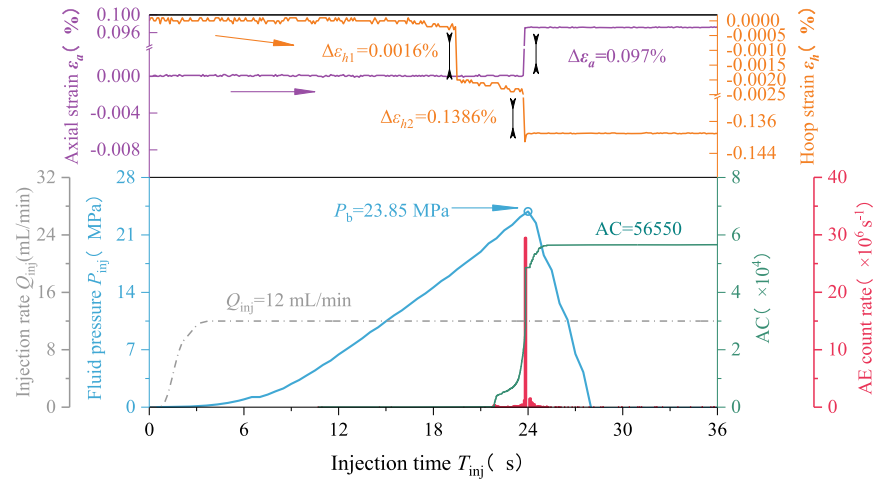

(b) Axial stress of 15 MPa (Sample CA-90-15)

Fig. 4.5 Evolution curves of pump pressure, rock deformation and AE under different axial stress states

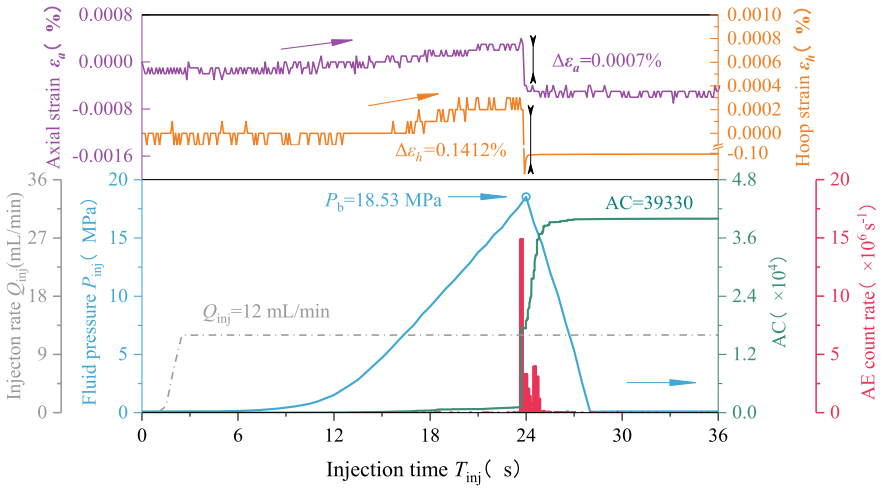

(c) Axial stress of 25 MPa (Sample CA-90-25)

Fig. 4.5 (continued)

stress, indicating that the AE activity decreases with the increase of initial axial stress during hydraulic fracturing.

The time-domain evolution of the dominant frequency and amplitude of AE during hydraulic fracturing is shown in Fig. 4.6. Similar to the preloading process, the low-frequency and low amplitude AE signals are produced in the hydraulic injection process. The low-frequency signals under different axial stress account for more than 87%, indicating that the tensile micro-cracks are mainly produced in hydraulic fracturing.

According to the time-domain distribution characteristics of the dominant frequency and amplitude of AE, the hydraulic fracturing process can be divided into three stages:

(1) Sporadic distribution stage of low frequency and low amplitude signals (stage i). This stage corresponds to the nonlinear pressure rise and energy storage process of the fluid in the borehole. The pump pressure transits from the initial slow

Table 4.1 Hydraulic fracturing parameters of shale samples under different axial stresses

Axial stress/MPa	Breakdown pressure P_b/MPa	Instantaneous strain increment /%		AE characteristic parameters	
		Circumferential $\Delta\varepsilon_h$	Axial $\Delta\varepsilon_a$	AC	Peak count rate (s^{-1})
5	28.27	0.127	0.0194	66,956	5.4×10^7
15	23.85	0.1386	0.0097	56,550	2.9×10^7
25	18.53	0.1412	−0.0007	39,330	1.5×10^7

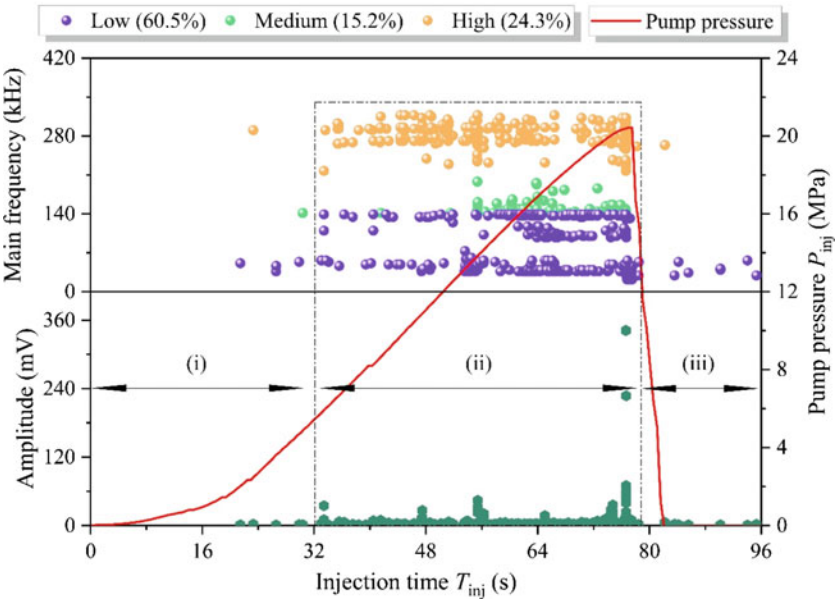

(a) Axial stress 5 MPa (Sample CA-90-5)

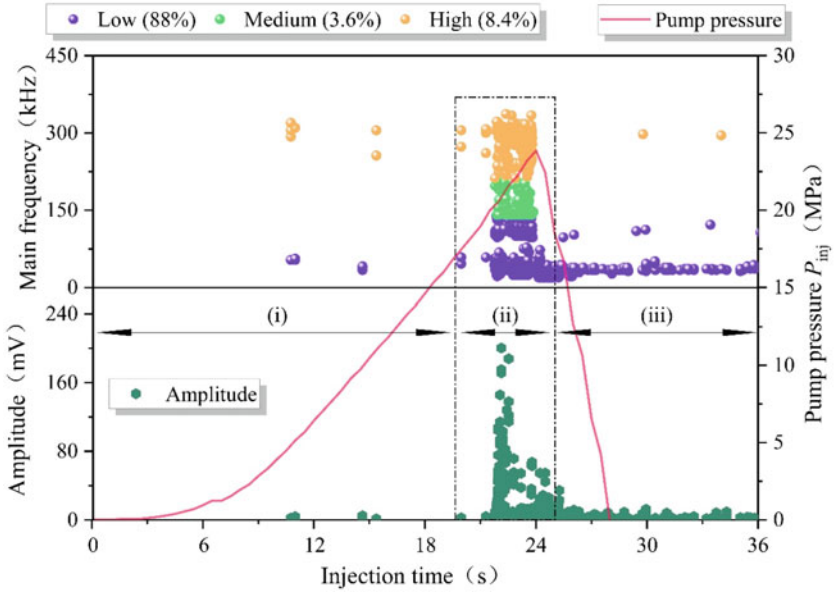

(b) Axial stress 15 MPa (Sample CA-90-15)

Fig. 4.6 Time–frequency characteristics of hydraulic injection process under different axial stresses

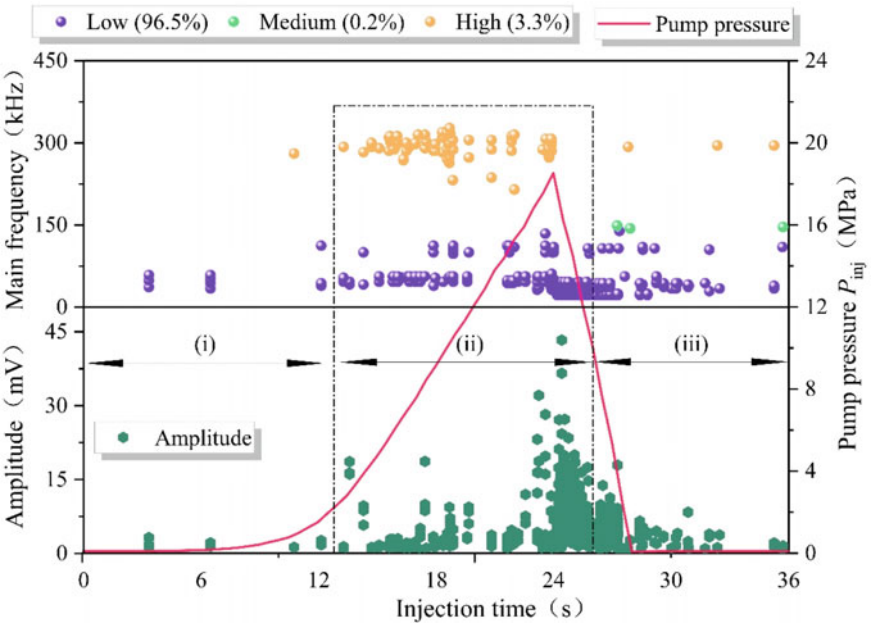

(c) Axial stress 25 MPa (Sample CA-90-25)

Fig. 4.6 (continued)

increase to the rapid and stable increase, and a small amount of high-frequency and low amplitude signals are generated during the injection process, indicating that the shear fracture could occur during the initial injection process.

(2) Intensive concentration stage of dominant frequency amplitude (stage ii). At this stage, the pump pressure keeps increasing rapidly and steadily until the breakdown pressure is reached. The sharply increased low and high-frequency double band high amplitude signals and medium frequency low amplitude signals appear at this stage and are densely distributed near the breakdown pressure, indicating that various types of micro-fractures are cracked, developed and connected before the breakdown of the sample, and the hydraulic fracturing process is accompanied by obvious high amplitude events.

(3) Stable extension stage of low frequency and low amplitude signals (stage iii). This stage corresponds to the pressure drop stage. The hydraulic fracture generated by fracturing provides a stable seepage channel for the fracturing fluid in the hole. Under the action of internal pressure, the fracturing fluid overflows along the hydraulic fracture, resulting in the rapid attenuation of pump pressure. When the overflow flow is equal to the injection flow, the pressure in the sample remains constant (0 MPa). Since then, the low-frequency and low amplitude AE signals monitored are mainly generated by the flow of fracturing fluid on the fracture and sample surface, which indicates that the constant flow of fluid

in the fracture may also generate low-frequency and low amplitude AE signals during hydraulic fracturing.

According to Fig. 4.6, when the axial stress is 5 MPa, the proportions of the high, medium, and low dominant frequency bands are 87.5%, 10%, and 2.5%, respectively; When the axial stress is 15 MPa, the high, medium and low dominant frequency bands are 88%, 3.6%, and 8.4%, respectively; When the axial stress is 25 MPa, the high, medium and low dominant frequency bands are 96.5%, 0.2%, and 3.3%, respectively. Comparing the proportions of various frequency bands under different Axial stress, it can be found that with the increase of axial stress, the proportion of low-frequency signals in the sample gradually increases, and the intermediate frequency signals gradually decrease, indicating that hydraulic fracturing under high axial stress promotes the generation of tensile micro fractures, and restrains the generation of shear fractures, especially tensile-shear mixed fractures.

To sum up, in the process of hydraulic fracturing, high local stress is generated around the borehole through constant flow pressurization, which promotes the radial expansion of the sample. When the pump pressure in the hole increases to the ultimate strength in a certain direction, the strain energy is released instantaneously, and the sample is fractured. When the axial stress is larger, the compaction effect of micro-cracks and pores in the sample is more obvious, and the breakdown pressure of the rock is lower. In addition, the increase of axial stress will promote tensile microfracture and inhibit the growth of tensile-shear mixed microfracture. It should be noted that the pressure corresponding to the high axial stress mentioned in this paper is less than 30% of the uniaxial compressive strength of the sample, that is, the axial stress applied will not generate macro-cracks in the sample. In addition, it is also noted that the pump pressure curve fluctuates obviously after the pump pressure reaches the breakdown pressure (such as sample CA-90-5). The reason is that the fluid pressure will be released with the fracture's propagation, and the fracturing fluid in the fracture will leak along the existing fracture, resulting in the closure of the fracture tip or even fracture arrest. Only by continuously increasing the pump pressure can the continuous crack initiation and propagation be maintained, thus causing the pump pressure to fluctuate.

② **Hydraulic fracture morphology**

(1) **Surface fracture morphology**

The fracture morphology on the sample surface under different axial stress is shown in Fig. 4.7. By referring to Ishida et al. [16] and Hou et al. [17], the fracture propagation path and morphology are depicted based on direct observation. In addition, the hydraulic fracture morphology is quantitatively characterized by the tortuosity [18], whose expression is

$$\tau = \frac{L}{l} \tag{4.1}$$

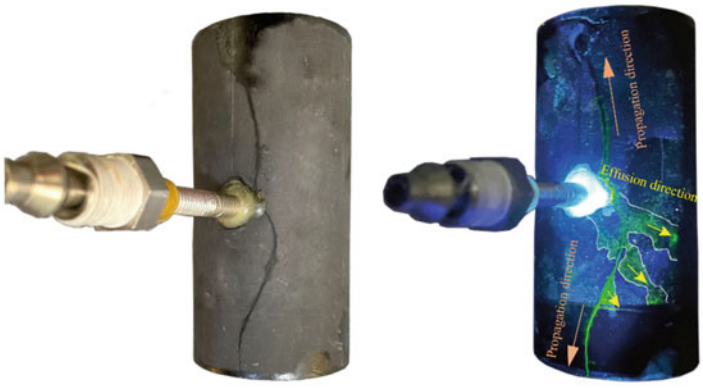

(a) Axial stress of 5 MPa (Sample CA-90-5)

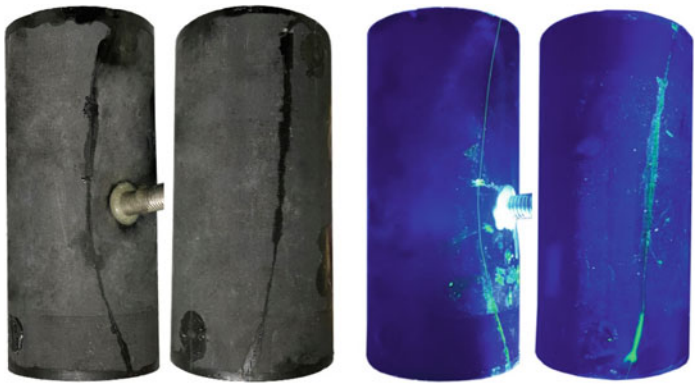

(b) Axial stress 15 MPa (Sample CA-90-15)

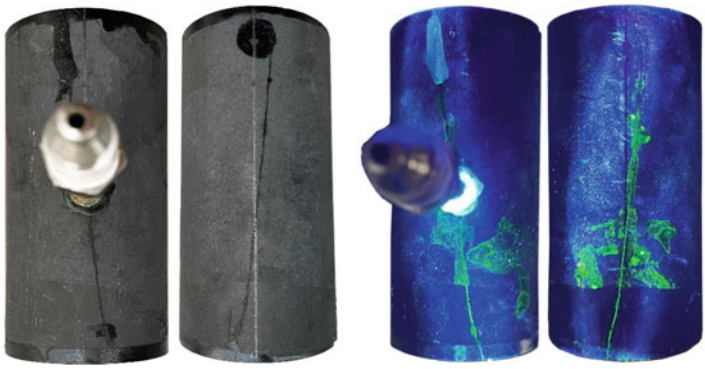

(c) Axial stress 25 MPa (Sample CA-90-25)

Fig. 4.7 Fracture morphology induced by hydraulic fracturing under different axial stresses (Left: natural light observation; Right: Ultraviolet light observation)

Table 4.2 Fracturing parameters under different axial stresses

Sample number	Axial stress σ_1/MPa	Injection rate Q_{inj}/mL/min	Tortuosity τ
CA-90-5	5	12	1.050
CA-90-15	15		1.028
CA-90-25	25		1.007

where τ represents the tortuosity, L is the actual length of the hydraulic fracture, and l is the distance between the two ends of the hydraulic fracture. The calculated tortuosity under different axial stresses is shown in Table 4.2. It should be noted that the tortuosity mentioned in this chapter is only for the main hydraulic fracture.

On the whole, no matter how the axial stress varies, the hydraulic fracture shows a bi-wing vertical propagation mode along both sides of the borehole. The axial stress has a certain disturbance on the fracture morphology of the sample surface. When the axial stress is 5 MPa, the hydraulic fracture initiates from the asymmetric position of the wellbore and then deflects in the direction of axial stress, and its morphology is tortuous ($\tau = 1.05$). With the increase of axial stress, the hydraulic fracture tends to be smooth gradually. When the axial stress increases from 5 to 15 MPa, the hydraulic fracture tortuosity decreases from 1.05 to 1.028, decreasing by 2.1%; When the axial stress continues to increase from 15 to 25 MPa, the tortuosity of the main fracture decreases from 1.028 to 1.007, decreased by 2%. This phenomenon shows that fracture tortuosity generally decreases with the increase of axial stress.

(2) **Roughness of fracture surface**

The roughness of the fracture surface is very important to evaluate the fluid flow and proppant migration in hydraulic fractures. The three-dimensional space coordinates x, y, and z (Fig. 4.8) of each point on the fracture surface can be acquired by the three-dimensional laser scanner and stored and output in text format so that the roughness parameters of the fracture surface can be calculated. The parameters used to quantitatively characterize roughness mainly include: the standard deviation of fracture surface height (SD) [19, 20], mean three-dimensional angle θ_s [21], and surface roughness coefficient R_s [22]. Three parameters have a certain correlation in their length scale, but they independently correspond to different physical meanings, which can characterize the morphological characteristics of rough fracture surfaces from different perspectives.

The standard deviation of fracture surface height (SD) refers to the standard deviation of the vertical height (i.e. z coordinate value) of each point on the fractured surface. SD is often used in geography to describe the topographic elevation degree. Here, it represents the fluctuation deviation degree of the concave-convex topography of the fracture surface. Its calculation formula is:

$$\mathrm{SD} = \sqrt{\frac{\sum_{i=1}^{N} (z_i - \overline{z})^2}{N - 1}} \tag{4.2}$$

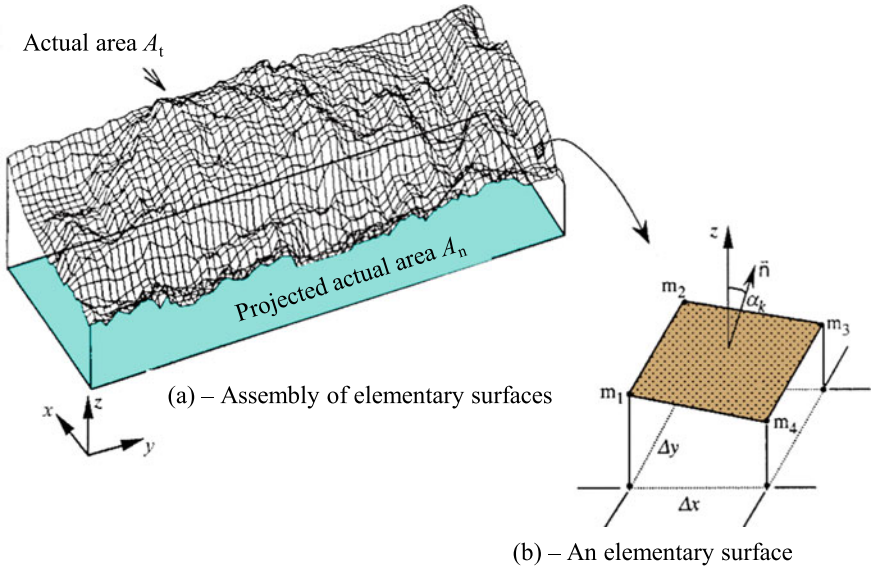

Fig. 4.8 Illustration of the calculating method of fracture toughness [22]

where N is the number of all coordinate points obtained from the fracture surface; Z_i is the Z coordinate value of the i_{th} coordinate point and $\overline{Z}$ the average value of the Z coordinates of all points.

Figure 4.9 is the standard deviation of fracture height and isoline cloud diagram of the main hydraulic fracture under different axial stress. It can be seen that SD decreases with increasing axial stress. When the axial stress is 5 MPa, the fracture surface is the roughest (SD = 2.79), with the highest height of 15.59 mm and the lowest height of −0.42 mm. When the axial stress increases to 15 MPa, the fracture surface is relatively flat, and the maximum and minimum heights of the fracture surface are 10.89 mm and 0.11 mm, respectively. When the axial stress reaches 25 MPa, the roughness of the fracture surface is the lowest, and the height of the fracture surface varies from 3.73 mm to 8.31 mm. These laws further show that increasing axial stress is beneficial for forming a straight hydraulic fracture.

The mean three-dimensional angle θ_s was first proposed by Belem et al. [21] and applied to evaluate the angular shape of the fracture surface. The calculation of θ_s should meet certain assumptions: the fracture surface is composed of a series of basic unit planes determined by the coordinate points on the fracture surface, as shown in Fig. 4.8. In Fig. 4.8, α_k refers to the angle between the normal vector of the basic unit plane and the Z coordinate axis. The θ_s is the arithmetic average of all α_k, and its calculation formula is:

$$\theta_s = \frac{1}{m} \sum_{i=1}^{m} (\alpha_k)_i \tag{4.3}$$

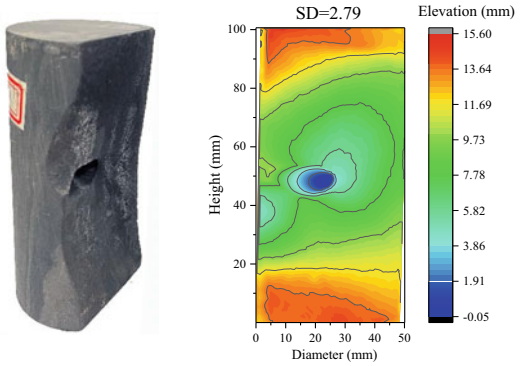

(a) Axial stress of 5 MPa (Sample CA-90-5)

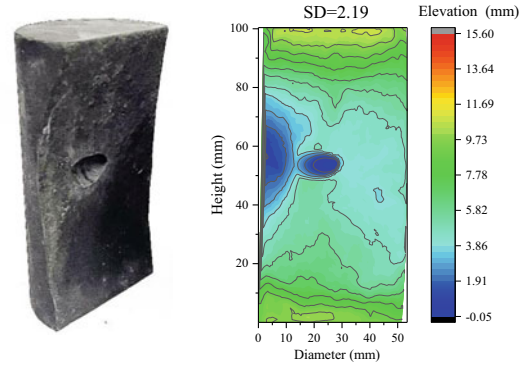

(b) Axial stress of 15 MPa (Sample CA-90-15)

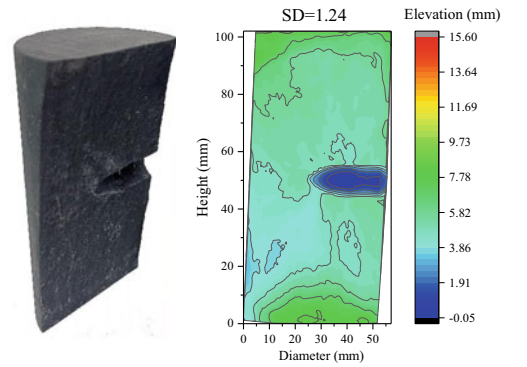

(c) Axial stress of 25 MPa (Sample CA-90-25)

Fig. 4.9 Contour maps of vertical hydraulic fractures in shale samples under different axial stresses

where m represents the number of basic element planes in the fracture surface.

The surface roughness coefficient R_s represents the roughness of the fracture surface, which is defined as the ratio of the true area of the fracture surface (A_t) to its normal projection area (A_n) (≥ 1). The calculation formula is:

$$R_s = \frac{A_t}{A_n} \tag{4.4}$$

According to Belem et al. [21], the true area of fracture surface (A_t) can be approximately calculated by the following formula:

$$A_t \approx (\Delta x \Delta y) \sum_{i=1}^{N_x - 1} \sum_{j=1}^{N_y - 1} \sqrt{1 + \left(\frac{z_{i+1,j} - z_{i,j}}{\Delta x} \right)^2 + \left(\frac{z_{i,j+1} - z_{i,j}}{\Delta y} \right)^2} \tag{4.5}$$

where Δx and Δy are constant calculation steps of the x-axis and the y-axis, respectively. According to the definition of R_s, the larger R_s corresponds to the larger the actual area of the fracture surface and the rougher fracture surface.

The mean three-dimensional angle and surface roughness coefficient of the fracture surface can be calculated by Eqs. (4.3) and (4.4), and the calculation results are shown in Fig. 4.10. It is easy to see that as the axial stress increases, θ_s and R_s are gradually decreased, indicating that the degree of angular undulation of the fracture surface is decreased and its flatness is increased. This law further confirms that increasing axial stress will promote the propagation of hydraulic fracture along the direction of maximum principal stress, and form a flat fracture with low roughness.

4.2.2 Effect of Injection Rate

The process of hydraulic fracturing in constant flow mode has obvious injection rate effect. Chitrala et al. [23] simulated the hydraulic fracturing process of Lyons sandstone reservoir through laboratory tests and found that a high injection rate induces high breakdown pressure. However, Zeng [24] thought that the high injection rate will reduce the breakdown pressure of the sample based on the hydraulic fracturing test of Jackfork sandstone and theoretical derivation and proposed a breakdown pressure model reflecting this relationship based on linear elastic fracture mechanics. Shao et al. [25] studied the effect of injection rate on breakdown pressure and pressurization rate by conducting true triaxial hydraulic fracturing tests. The results show that with the injection rate increase, breakdown pressure increases nonlinearly, but the increase rate decreases gradually. In addition, it is also found that the injection rate has a linear positive correlation with the hydraulic pressurization rate in the stable pressurization stage. On the premise of considering the anisotropy of granite and ignoring the confining pressure disturbance, Zhuang et al. [26] carried out uniaxial hydraulic fracturing tests with the aid of AE and CT scanning. It is found that the

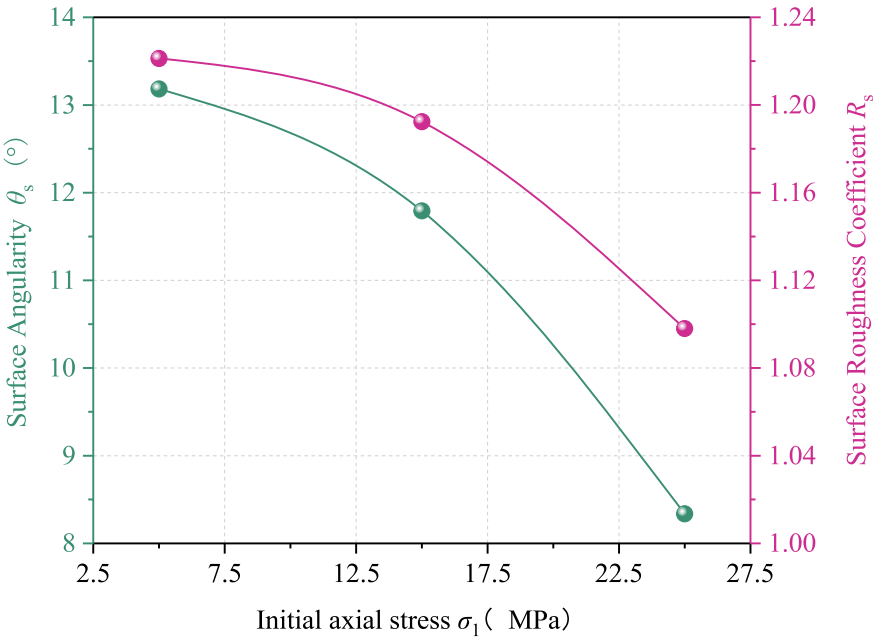

Fig. 4.10 Evolution of mean three-dimensional angle and roughness coefficient of fracture surfaces under different axial stresses

effect of injection rate on the hydraulic fracturing process has the characteristics of stage threshold. When the injection rate is lower than the critical threshold, the hydraulic pressure in the hole increases slowly, and the water permeates into the rock matrix, resulting in the sample finally reaching the fully saturated state without being fractured. When the injection rate is greater than the critical threshold, the pump pressure in the hole increases rapidly until hydraulic fracturing occurs, and the critical breakdown pressure increases with the increase of the injection rate.

According to the above research status, the disturbance of injection rate on the hydraulic fracturing process is mainly reflected in the following two aspects: (1) the effect of injection rate on the change of pressurization rate. Generally speaking, a high injection rate will produce a high pressurization rate and induce a strain rate effect, leading to a rapid increase of pore pressure gradient around the borehole during hydraulic pressurization and promoting rock fracture. (2) The injection rate is closely related to the hydraulic infiltration process. At a low injection rate, the hydraulic pressurization process takes a long time, and the fluid permeates into the rock matrix, which is mainly affected by the permeability of the sample and the pressurization time; On the other hand, when the injection rate is high, the pressure increases rapidly, resulting in hydraulic fracturing of the sample before infiltration.

However, previous studies have not analyzed and discussed the evolution law of microfracture during hydraulic fracturing under different injection rates, so there is a lack of explanation of the mechanism of injection rate on microfracture during

hydraulic fracturing. In this section, combined with AE and strain, the hydraulic fracturing results at injection rates of 3, 6, 12, 18 and 30 mL/min are mainly analyzed to explore the disturbance mechanism of different injection rates on the microfracture process of rocks.

① **Evolution of pump pressure, deformation and AE**

The evolution law of the pump pressure, deformation and AE of the sample under different injection rates is shown in Fig. 4.11. Comparing Fig. 4.11a–e, it can be seen that under different injection rates, the evolution trends of pump pressure, deformation and AE are relatively consistent, that is, with the continuous increase of pump pressure, the change of circumferential strain (in numerical value) of each sample shows a nonlinear increase, while the axial strain basically does not change. At the same time, the signal accumulation rate of AE counting is gradually accelerated. When the pump pressure is close to the breakdown pressure, the AE counting rate reaches the peak first. After about 0.1 ~ 0.3 s, the circumferential strain increases sharply, the axial strain decreases abruptly, and the pump pressure decays rapidly to zero.

Comparing the curves under five injection rates, it can be found that with the increase of injection rate, the time for hydraulic fracturing of the sample is shortened and the breakdown pressure (P_b) is increased, which is consistent with the test results of Haimson [27], Zoback [28] and Solberg [29].

In addition, different injection rates have different effects on the deformation of the samples during hydraulic fracturing. When the injection rate is low (Q_{inj} = 3 mL/min), the axial and circumferential strains of the sample increase slowly during the injection pressurization process. Until the sample is broken, the axial and circumferential strains are almost constant, and the volume strain increment at the critical failure is 0.0881% (Fig. 4.11a). However, for the sample with Q_{inj} = 6 mL/min, when the pump pressure increases to 10 MPa, the circumferential strain increases abnormally ($\Delta\varepsilon_{h1} = 0.0009\%$), which may be caused by the sudden release of high pump pressure accumulated in the borehole due to local fracture in the sample (Fig. 4.11b).

Unlike the experimental results with an injection rate of 3 mL/min, the circumferential strain of the sample with an injection rate of 6 mL/min keeps a stable decreasing trend before fracturing, and at the moment of fracturing, the instantaneous volume strain increment of the sample reaches 0.1275%. When the injection rate is 12 mL/min, the circumferential strain of the sample will show an obvious nonlinear downward trend with the pump pressure increase, and the volumetric strain at the time of failure is 0.2734%, as shown in Fig. 4.11c. When the injection rate is 18 mL/min or 30 mL/min, the axial strain of the sample is basically constant during the hydraulic pressurization process, and the circumferential strain shows a significant increasing trend (obvious lateral expansion). At the moment of fracturing, the volume strain increment of the two injection rates is 2.0951% and 2.938%, respectively. Overall, the injection rate's effect on the sample's deformation process is mainly reflected in the initial pressurization and instantaneous fracturing stages. The deformation of the sample after complete fracturing is no longer disturbed by the injection rate.

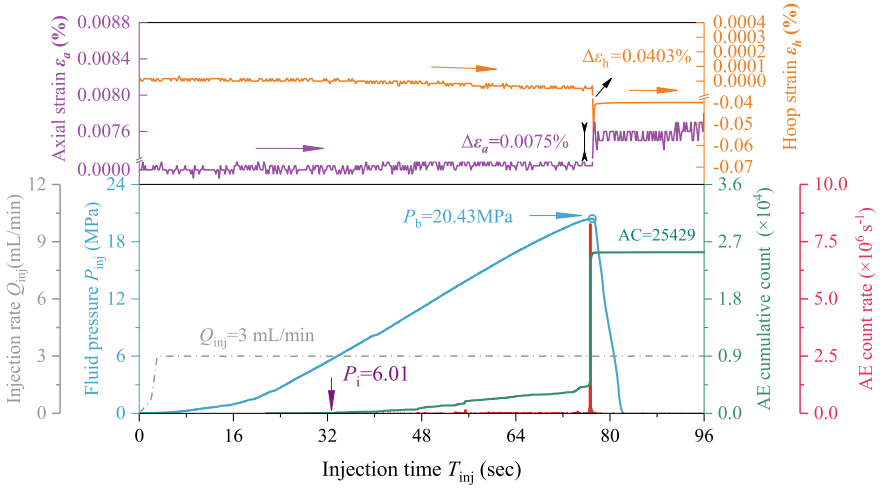

(a) Q_{inj} = 3 mL/min (Sample CI-90-3)

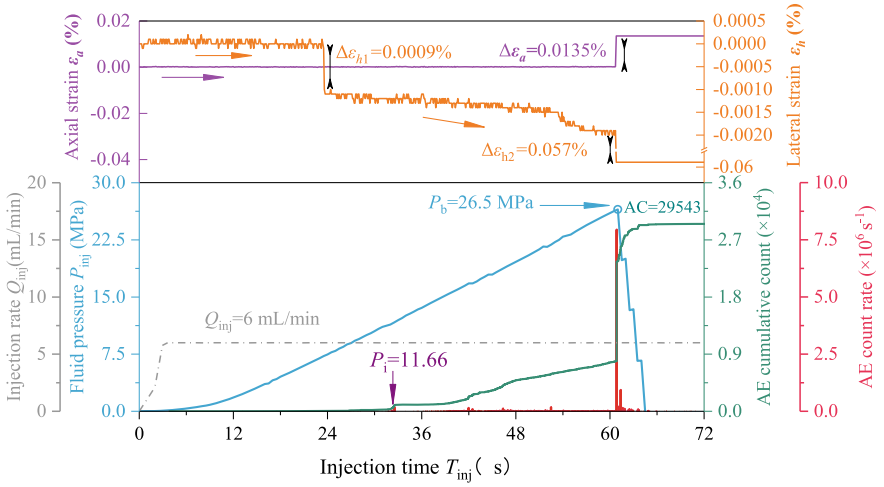

(b) Q_{inj} = 6 mL/min (Sample CI-90-6)

Fig. 4.11 Evolution curves of pump pressure, rock deformation and AE under different injection rates

In the process of hydraulic pressurization, with the increase of injection rate, the radial expansion deformation of samples before fracturing tends to be more obvious. At the moment of fracturing, the volume strain at critical failure also gradually increases with the injection rate increase. This phenomenon can be explained from the perspective of energy, that is, a high injection rate will accumulate higher strain

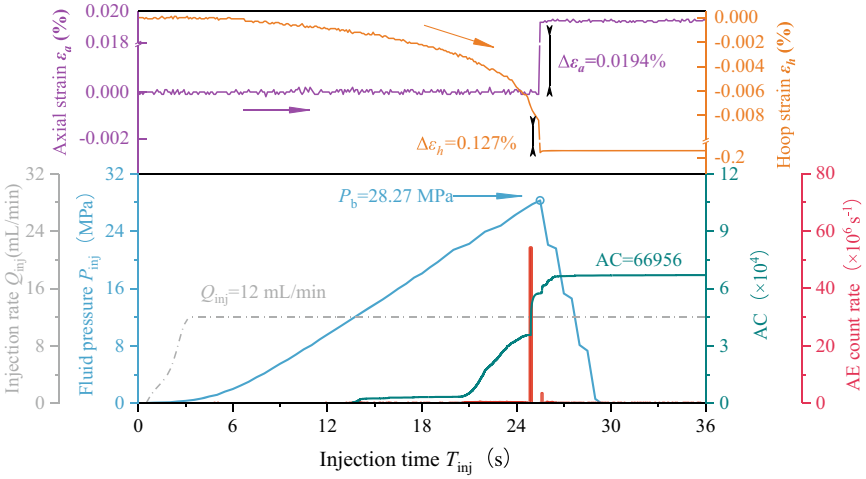

(c) Q_{inj} = 12 mL/min (Sample CA-90-12)

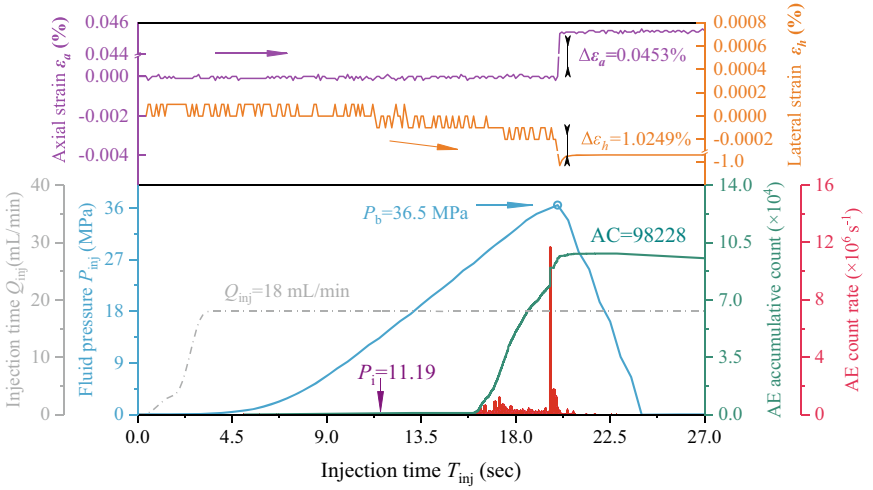

(d) Q_{inj} =18 mL/min (Sample CI-90-18)

Fig. 4.11 (continued)

energy, resulting in the release of more energy during fracturing, which induces the sample to produce greater volume strain. This conclusion is further confirmed by the increase of AE cumulative counts with the injection rate increase during fracturing, as shown in Fig. 4.11a–e.

There are also differences in damage accumulation and fracture mode evolution under different injection rates. Comparing Fig. 4.11a–e, it can be found that with the

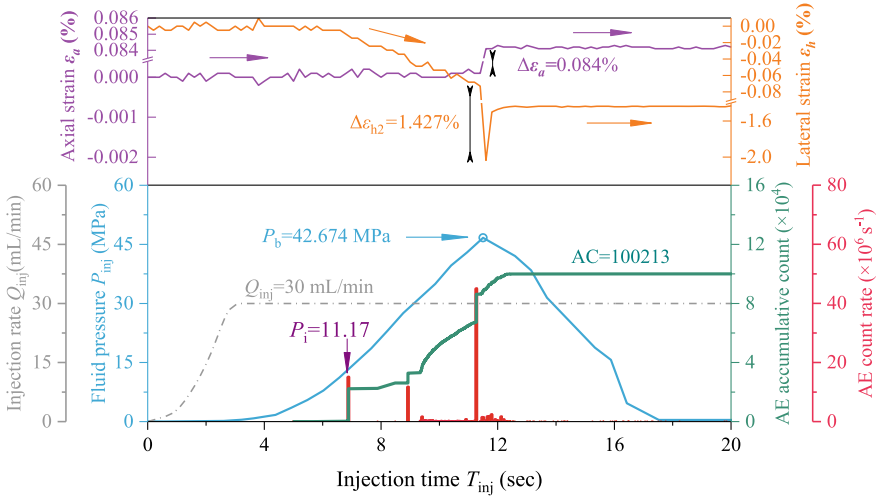

(e) Q_{inj} = 30 mL/min (Sample CI-90-30)

Fig. 4.11 (continued)

increase of injection rate, the growth rate of AE cumulative counts gradually accelerates. Specifically, when the injection rate is low, the AE count generally shows a changing trend of slowly increasing at first and then rapidly increasing. The accumulation of AE signals has a transient change, as shown in Fig. 4.11a–c. With the increase of injection rate ($Q_{inj} \geq 18$ mL/min), the slow growth section of AE cumulative counts is significantly shortened. The count signal increases rapidly in the preloading stage before critical failure. In contrast, the AE count released during fracturing is relatively small, indicating that a high injection rate will aggravate the development of microfracture and promote the propagation and penetration process of microfracture. In addition, the AE count rate gradually fluctuates significantly in the hydraulic pressurization stage. Especially when the injection rate is 30 mL/min, there are two independent peaks in the count rate before fracturing, indicating that there are two fractures cracking in the sample. The initiation of a new fracture may lead to pressure loss at the crack tip, so it is necessary to further increase the pump pressure, which will eventually lead to the unstable propagation of the fracture, resulting in a higher breakdown pressure [28].

Table 4.3 records the breakdown pressure, deformation and AE characteristic parameters at different injection rates. It can be seen that the instantaneous strain, AE cumulative counts and peak count rate of the sample are positively correlated with the injection rate. It should be noted that the peak count rate does not strictly increase with the injection rate, which may be due to the difference of individual physical properties of the sample or the uneven distribution of micro cracks, resulting in the difference of the cracking degree of the sample.

Table 4.3 Fracturing results at different injection rates

Injection rate (mL/min)	Breakdown pressure P_b (MPa)	Instantaneous strain increment /%		AE characteristic parameters	
		Circumferential $\Delta\varepsilon_h$	Axial $\Delta\varepsilon_a$	Accumulative AC	Peak count rate (s^{-1})
3	20.43	0.0403	0.0075	25,429	0.82×10^7
6	26.5	0.057	0.0135	29,543	0.74×10^7
12	28.27	0.127	0.0194	66,956	5.4×10^7
18	36.5	1.0249	0.0453	98,228	1.17×10^7
30	42.674	1.427	0.084	100,213	4.51×10^7

Microfracture initiation pressure refers to the pump pressure corresponding to the time when the AE activity starts to change significantly during hydraulic fracturing [28]. The fracture initiation pressure of the sample under different injection rates has been marked in Fig. 4.11, and its magnitude relative to the breakdown pressure and its variation with the injection rate is shown in Fig. 4.12. Compared with the breakdown pressure, the fracture initiation pressure is smaller. When the injection rate is greater than 6 mL/min, the fracture initiation pressure is no longer sensitive to the change of the injection rate. The difference between the two pressures increases with the increase of the injection rate.

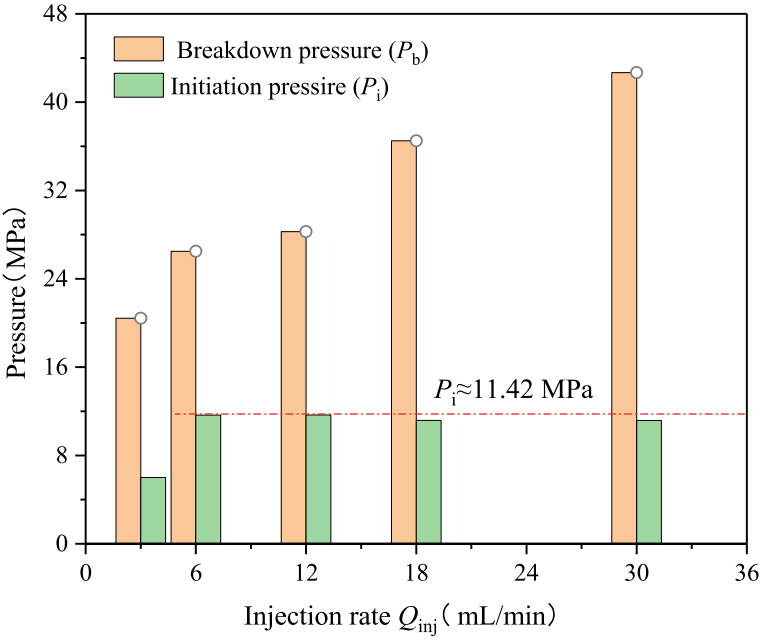

Fig. 4.12 Breakdown pressure and fracture initiation pressure under different injection rates

Figure 4.13 shows the time–frequency evolution of AE during hydraulic injection at different injection rates. Comparing Fig. 4.13a–e, it can be seen that the proportion of low-frequency AE signals generated by hydraulic fracturing at each injection rate is more than 60%, indicating that the hydraulic fracturing process mainly produces tensile micro-fractures, which is less affected by the injection rate. In contrast, the ratio of shear type (high-frequency band) AE signal is more sensitive to the change of injection rate. When the injection rate is low (3 and 6 mL/min), the high-frequency signals of shear fracture produced by hydraulic pressurization account for 24.3% and 17.9%, respectively. With the increase of injection rate (12, 18, and 30 mL/min), the shear type high-frequency band signal is gradually decreasing (2.5%, 3.6%, and 3.3%, respectively), indicating that a high injection rate is more prone to produce tensile microcracks and a low injection rate promote the generation of shear microcracks. The influence of injection rate on the time-domain distribution of dominant frequency amplitude is mainly reflected in the dense concentration section (ii). It is easy to see that with the increase of the injection rate, the dominant frequency time domain gradually presents a zonal characteristic, that is, the dominant frequency is concentrated at the beginning and end of the dense concentration section (ii), while the AE signal is less at the middle position. The above phenomenon is because this period corresponds to the linear pressurization process, and the sample is approximately in the elastic stage, so the micro crack initiation and penetration activities are less.

Overall, the higher the injection rate, the more low-frequency and high amplitude signals are induced, and the more tensile micro fractures are generated. In addition, for Longmaxi shale with low permeability and high brittleness, the change of injection rate will not affect the overall fracture type of rock. In other words, no matter how the injection rate changes, the microfractures induced by hydraulic fracturing are still mainly tensile fractures, which account for more than 60%. However, Chitrala et al. [30] found in the tests that shear failure induced by hydraulic fracturing usually occurs at low and medium injection rates (0.5–5 mL/min), while tensile fracture occurs at a high injection rate. This conclusion seems to contradict the current experimental results. However, it should be noted that there are essential differences between the two test materials. Chitrala et al. [30] explored the injection rate effect based on Lyons sandstone samples, with a permeability of 10 μD, which is almost 100 times of permeability of the rock used in this experiment. Therefore, in the hydraulic fracturing test with low and medium injection rates, the influence of local leakage of Lyons sandstone is obviously greater than that of the current shale. When the fluid infiltrates into the sandstone matrix, the pore pressure around the wellbore increases, and the effective stress decreases significantly, which is more likely to promote the local sliding of micro fractures and produce shear fractures. On the other hand, it is also found in the current test that when the injection rate is low, the high-frequency shear signal generated in the fracturing process is significantly increased, indicating that a low injection rate will be conducive to generating micro shear fracture in the sample. However, whether the shear fracture finally occurs in the sample still depends on the physical and mechanical properties of the rock. Moreover, in-situ stress, temperature, fluid viscosity, et al., may have complex effects on rock fracture

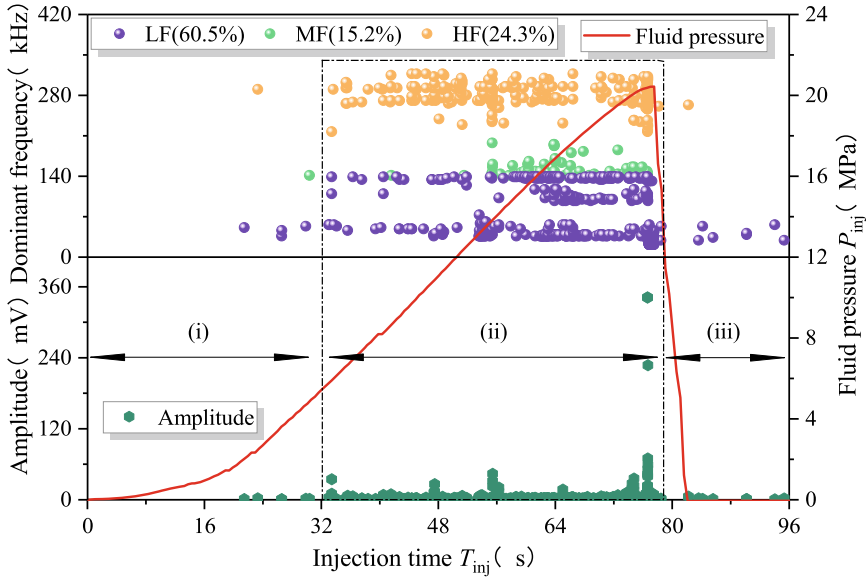

(a) Q_{inj}=3 mL/min (Sample CI-90-3)

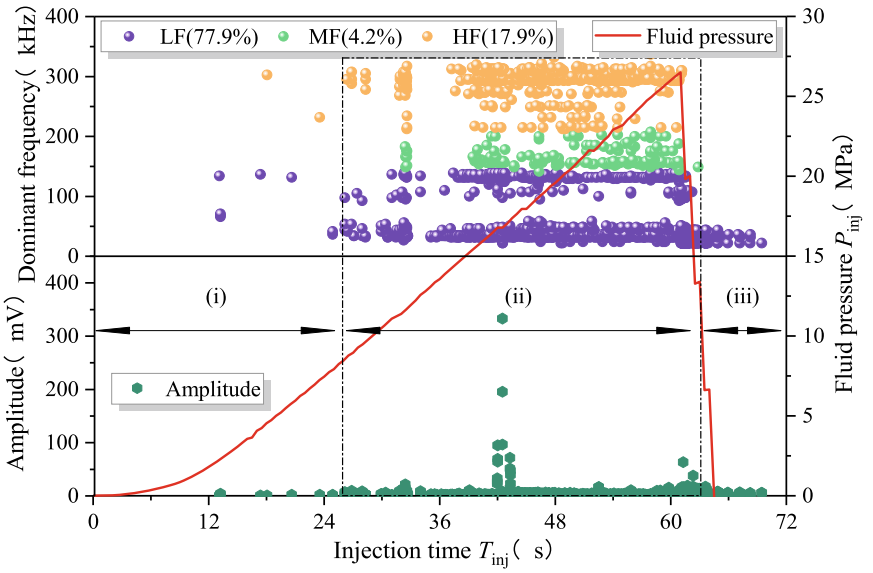

(b) Q_{inj}=6 mL/min (Sample CI-90-6)

Fig. 4.13 Time–frequency characteristics of hydraulic injection process under different injection rates

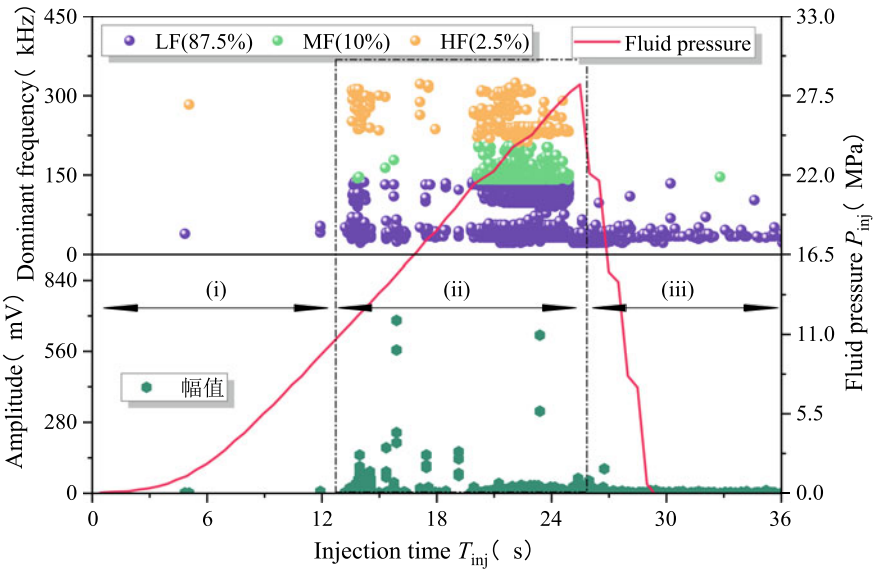

(c) Q_{inj}=12 mL/min (Sample CI-90-12)

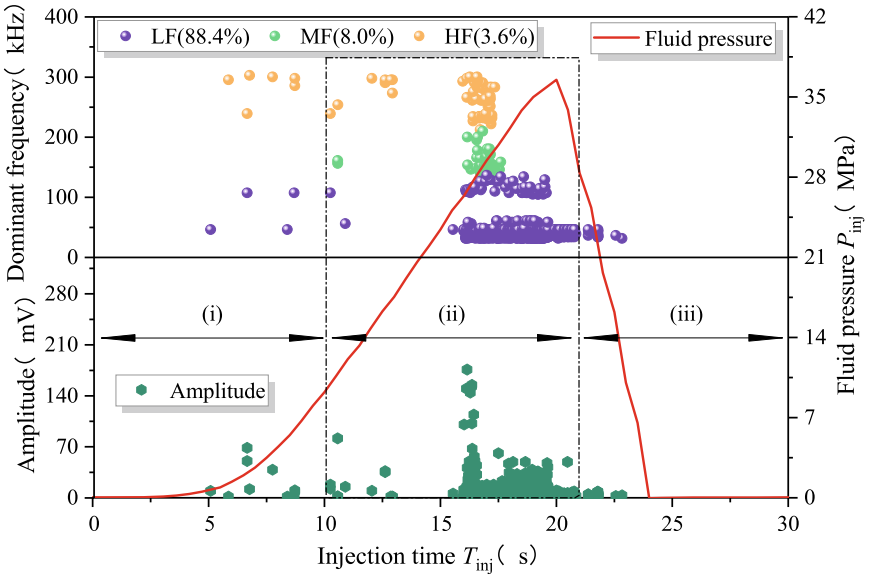

(d) Q_{inj}=18 mL/min (Sample CI-90-18)

Fig. 4.13 (continued)

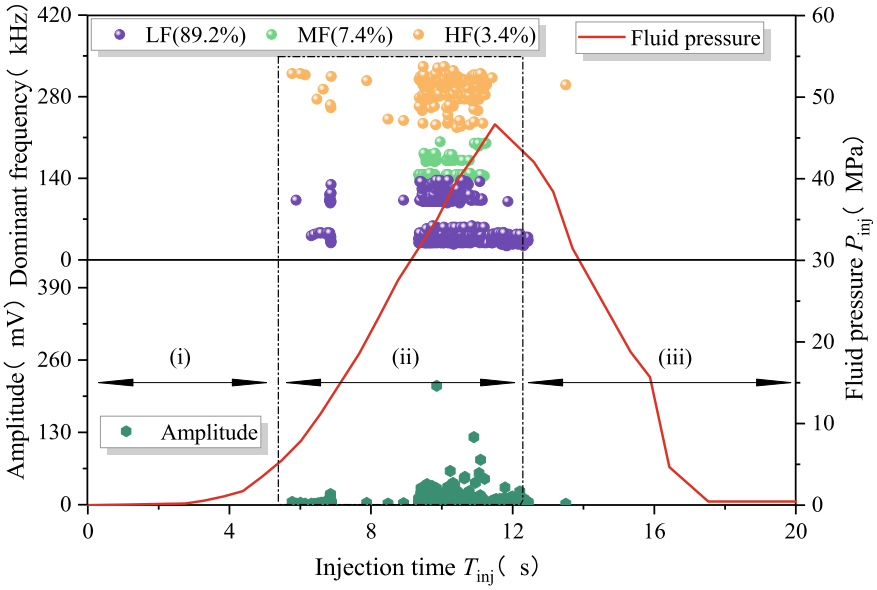

(e) Q_{inj}=30 mL/min (Sample CI-90-30)

Fig. 4.13 (continued)

mode, and these factors are still worth further discussion. Nevertheless, the current test results can still provide some reference for directional control of fractures and evaluation of fracture morphology through injection rate in actual fracturing design.

② **Evolution of pressurization rate**

Pressurization rate refers to the increase rate of pump pressure per unit of time, which is mainly related to sample size, wellbore size and injection rate [1]. As we all know, the larger the injection rate, the faster the fluid pressurization, and the more intense the evolution of the pressurization rate. Under the premise of ignoring permeability, this parameter is a physical quantity to measure the speed of hydraulic pressurization in the wellbore.

Figure 4.14 is the time-varying curve of the pressurization rate during hydraulic fracturing before fracturing under different injection rates. The abscissa of the symbol at the end of the curve corresponds to the time of the fracturing moment. It can be seen from Fig. 4.14a that the evolution trend of the pressurization rate with time is similar under different rates. Taking sample CI-90–12 as an example (see Fig. 4.14b), the pressurization rate goes through three stages in total. The pressurization rate increases monotonously at the beginning (stage A), then remains constant (stage B), and gradually decreases near the breakdown pressure (stage C). The pressurization rate at different rates has a maximum value in stage B. However, the difference is that when the rate is low (Q_{inj} = 3 and 6 mL/min), the evolution process of the pressurization rate before fracturing is relatively gentle. At the same time, for the

high injection rate ($Q_{inj} = 12 \sim 30$ mL/min), the pressurization rate increases rapidly in stage A, then keeps fluctuating in stage B, and drops quickly in critical fracturing. These phenomena become more obvious with the increase of the injection rate.

To evaluate the relationship between injection rate and pressurization rate, the average value of pressurization rate in stage B is used to reflect the pressurization effect of injection rate. It can be calculated from Fig. 4.14 that when the injection rate is 3, 6, 12, 18, and 30 mL/min, the corresponding stable pressurization rate is 0.353, 0.74, 1.458, 2.392, and 6.412 MPa/s, respectively, indicating that the pressurization rate increases with the increase of the injection rate. However, from the change law of the stable pressurization rate relative to the injection rate (Fig. 4.15), different from the previous test results [25–31], the stable pressurization rate and the injection rate do not maintain a strict linear relationship but are in the form of a quadratic polynomial ($R^2 = 0.997$). The nonlinear relationship between stable pressurization rate and injection rate was also verified in the experiment of Chitrala et al. [30]. As shown in Fig. 4.15, it can be found by fitting that the quadratic polynomial relationship is also suitable for Chitrala's test results ($R^2 = 0.998$). The reason why the stable pressurization rate does not maintain a strictly linear relationship with the injection rate may be that the fluid is compressed to a certain extent during the hydraulic pressurization process and may also be related to the wellbore size, permeability of reservoir rock, fracture distribution, temperature, in-situ stress [32, 33]. It should be noted that because the Lyons sandstone is selected as the research object in the test of Chitrala et al. [30], and the Longmaxi shale is selected as the research object in the current test, the relationship between the pressurization rate and the injection rate does not meet the same binomial formula. Nevertheless, considering the compressibility of liquid and the permeability of rock, this nonlinear relationship is more suitable for the actual hydraulic fracturing process.

③ Fracture morphology

(1) Fracture surface morphology

Figure 4.16 shows the fracture morphology of shale samples under different injection rates. By comparing the calculation results of fracture morphology under different injection rates (see Table 4.4), it can be found that with the increase in injection rate, the fracture morphology on the surface of the sample gradually changes from a branched and twisted fracture to a single bi-wing fracture. This phenomenon is caused by the fact that under the low injection rate ($Q_{inj} = 3 \sim 6$ mL/min), the fluid is more likely to penetrate the weak bedding plane, resulting in the increase of pore pressure and the decrease of effective stress, which makes it easier to slip or activate secondary fractures. Under the continuous action of the pump pressure, the fluid will have sufficient time to penetrate into the secondary fractures, thus leading to the propagation and penetration of the fractures at all levels, forming a tortuous and complex fracture morphology. When the injection rate is high ($Q_{inj} = 12 \sim 24$ mL/min), the pump pressure increases rapidly, and the fluid cannot fully penetrate into the primary defects and structural planes. When the local fracture cracks, the high pressure accumulated in the wellbore will be directly released through the

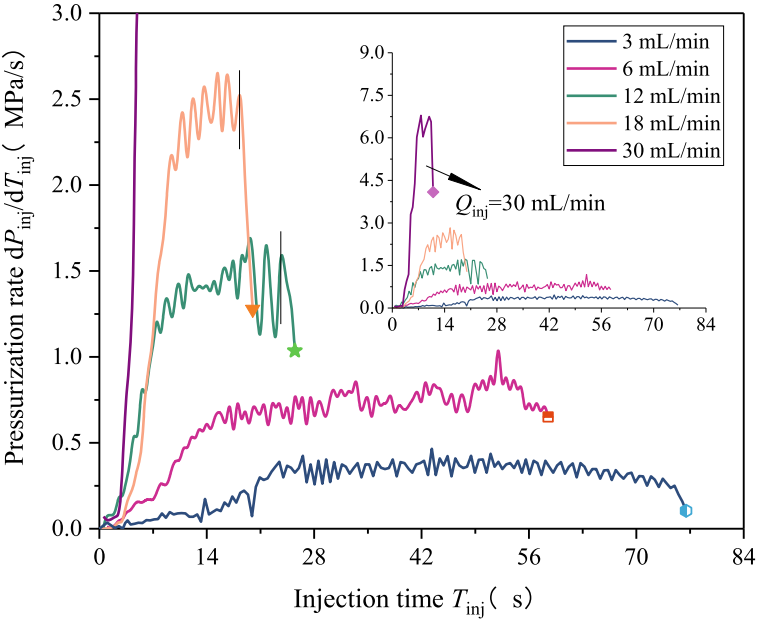

(a) Comparison of pressurization rate under different injection rates

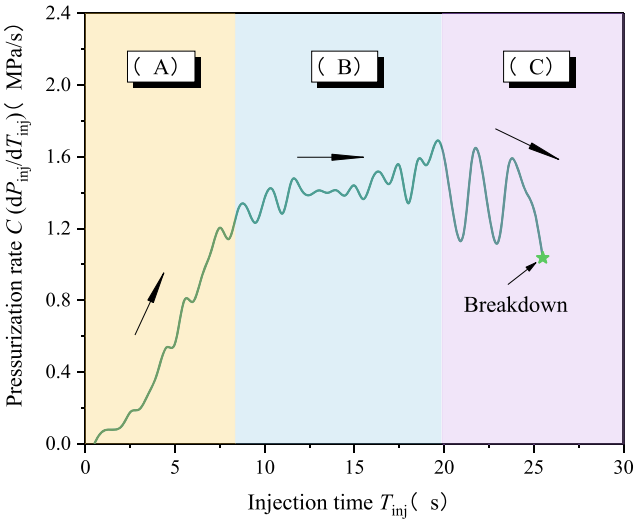

(b) Sample CI-90-12 (Q_{inj}=12 mL/min)

Fig. 4.14 Curves of pressurization rate versus time (the signs at the end of the curves represents the time when the breakdown occurs)

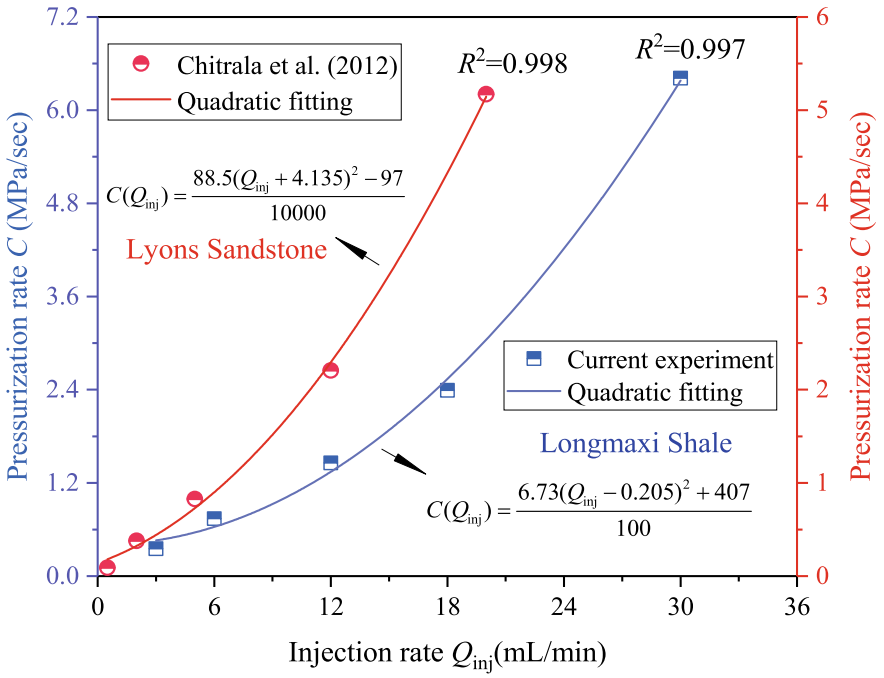

Fig. 4.15 Relationship between pressurization rate and injection rate

fracture, which induces the hydraulic fracture to propagate along its mechanically preferable direction (i.e., the direction of the maximum principal stress), forming a simple fracture. In addition, it can also be found that when the injection rate is lower than 6 mL/min, the angle between the hydraulic fracture and the bedding plane is approximately 60°, indicating that a low injection rate is conducive to inducing tortuous hydraulic fractures. This phenomenon may be due to the fact the axial preloading and fluid injection process produce more shear micro-fractures in the sample. At a low injection rate, the fracturing fluid has more time to infiltrate into the micro-fractures of the matrix, resulting in local shear along the original defects and disturbing the main hydraulic fracture to deviate from the initial fracture initiation direction, forming a tortuous fracture.

A stereomicroscope was used to observe the local fracture propagation morphology and measure the fracture width to further study the detailed characteristics of hydraulic fracture propagation under different injection rates. Taking the samples with an injection rate of 3 mL/min and 30 mL/min as examples, the results are shown in Fig. 4.17. It can be seen that in hydraulic fracturing with a low injection rate, the main fracture produces two branch fractures. One branch fracture (branch 1) still propagates along the initial direction, but the fracture width gradually decreases. The other branch fracture generates local shear (green arrow position), leading to a

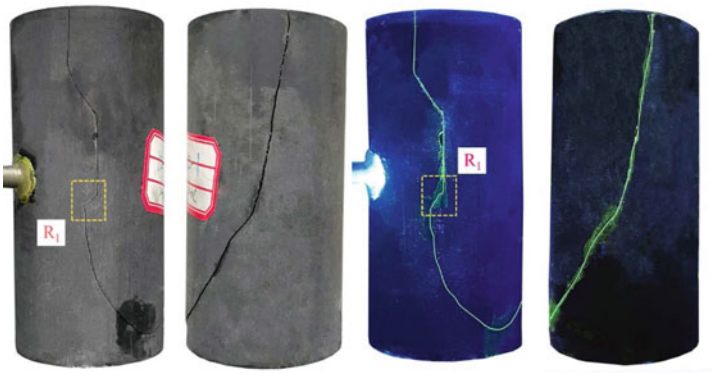

(a) Q_{inj}=3 mL/min (Sample CI-90-3)

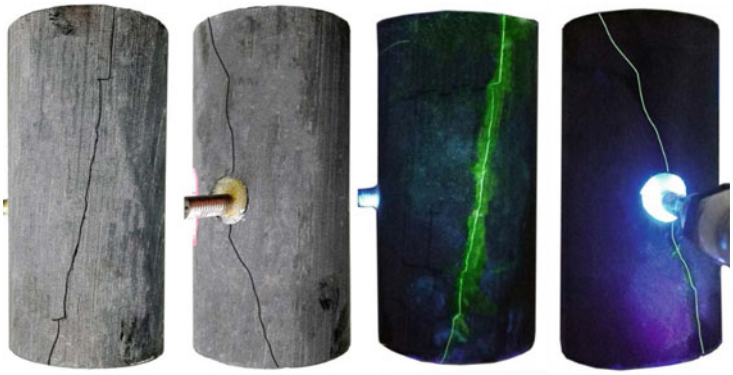

(b) Q_{inj}=6 mL/min (Sample CI-90-6)

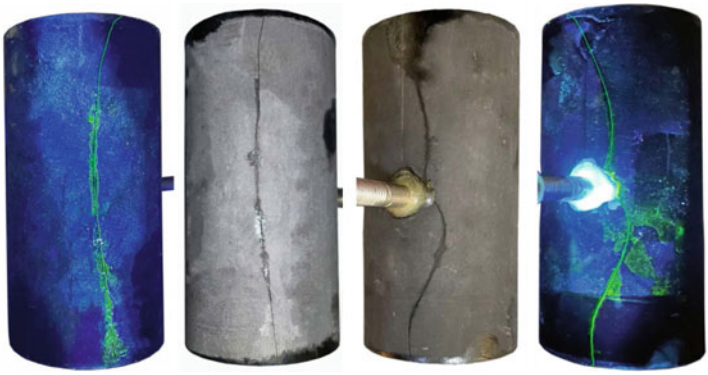

(c) Q_{inj}=12 mL/min (Sample CI-90-12)

Fig. 4.16 Surface fracture morphology under different injection rates

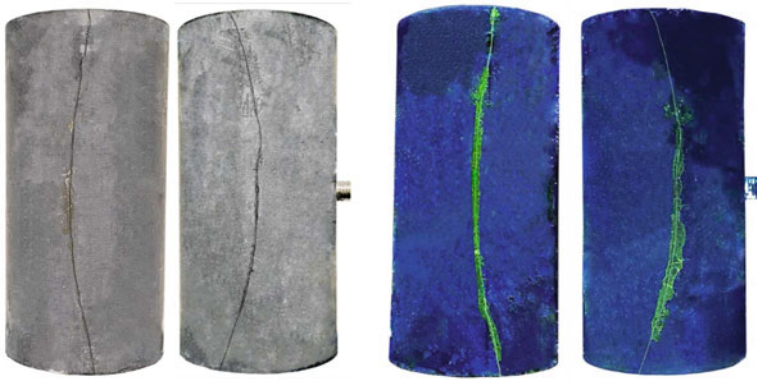

(d) Q_{inj}=18 mL/min (Sample CI-90-18)

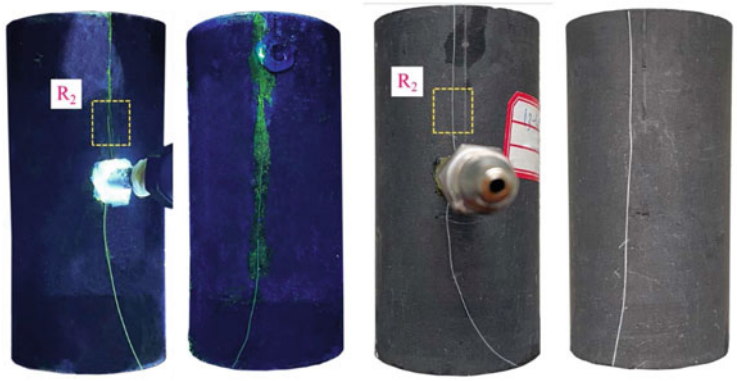

(e) Q_{inj}=30 mL/min (Sample CI-90-30)

Fig. 4.16 (continued)

Table 4.4 Fracture tortuosity under different injection rates

Sample	σ_1/MPa	Injection rate Q_{inj}/mL/min	Tortuosity τ
CI-90-3	5	3	1.231
CI-90-6		6	1.112
CI-90-12		12	1.028
CI-90-18		18	1.023
CI-90-30		30	1.016

certain degree of deflection in the main fracture path. However, the final propagation direction of the main fracture is still consistent with the main fracture direction before shear slip (i.e., along the direction of the maximum principal stress), further confirming the previous inference that a low injection rate is conducive to inducing microfracture and shear slip. It should be noted that although the residual fracture

width after the test may differ from the fracture width under dynamic loading of stress and pump pressure, the evolution of the fracture width can still provide some reference for analyzing the fracture propagation process [34]. Comparing the change of fracture width before and after the fracture branching, it can be found that the total width of the fracture after branching is reduced. The above phenomenon is because after the local shear slip occurs, the concave and convex bodies on the two staggered sections support each other, which forms the residual pore diameter to provide a channel for the internal fluid overflow [35], promoting the local injection energy loss, and reducing the fracture cracking effectiveness. In addition, after the slip, branch 2 gradually evolves into the main crack and continues to propagate, while the opening of branch 1 decreases until it stops propagating, which indicates that the local slip behavior of branch 2 impedes the subsequent propagation of branch 1. Similar conclusions can also be found in the experimental study of Zhao et al. [36]. With the increase of injection rate, the morphology of hydraulic fracture tends to be single and straight, the direction of fracture propagation coincides with the direction of maximum principal stress, and the width of fracture keeps approximately the same.

(2) **Three-dimensional fracture morphology**

Figure 4.18 shows fracture morphology and standard deviation of fracture elevation after hydraulic fracturing under different injection rates. From the fracture surface morphology of the sample, it can be seen that with the increase of the injection rate, the fracture surface gradually changes from a shear slip surface propagating obliquely to a tensile fracture surface propagating vertically, which further confirms that the low injection rate is conducive to inducing shear cracks in the sample. In addition, when the injection rate is increased from 3 mL/min to 30 mL/min, the standard deviation of fracture surface elevation is reduced from 4.63 to 2.38, indicating that with the increase of injection rate, the lower the standard deviation of fracture surface elevation is, the rougher the fracture surface is. In fact, the relationship between the standard deviation of surface elevation and injection rate is nonlinear. For example, when the injection rate is 6 mL/min, the maximum and minimum elevations of the fracture surface are 18.03 mm and 2.15 mm respectively, and the elevation contrast of the fracture surface is 4.06, which is 12.3% lower than that of 3 mL/min. When the injection rate is 12 mL/min, the maximum and minimum elevations of the fracture surface are 15.59 and −0.04 mm. Compared with 6 mL/min, the maximum and minimum elevations of 12 mL/min are reduced, and the standard deviation is 2.79, which is 31.3% lower than that of 6 mL/min. When the injection rate increased to 18 mL/min, the maximum and minimum elevations of the fracture surface became 15.45 mm and 0.01 mm, while the standard deviation of surface elevation decreased to 2.57, which decreased by 7.9% compared with the injection rate of 12 mL/min. When the injection rate is further increased to 30 mL/min, the maximum elevation of the fracture surface of the sample is 11.59 mm, the minimum elevation is 1.29 mm, and the standard deviation of elevation is 2.38, which is only 7.4% lower than that at an injection rate of 18 mL/min. These laws indicate that the disturbance effect of injection rate on fracture surface morphology is limited. Within the limited injection

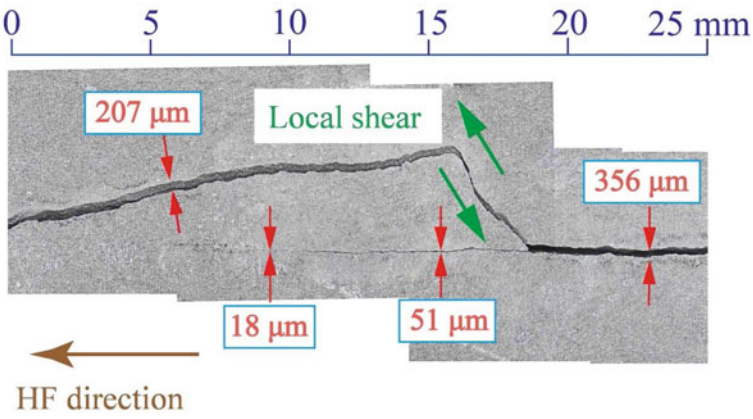

(a) Q_{inj}=3 mL/min，Sample CI-90-3 (corresponding to details at R_1 in Fig. 4.16 (a))

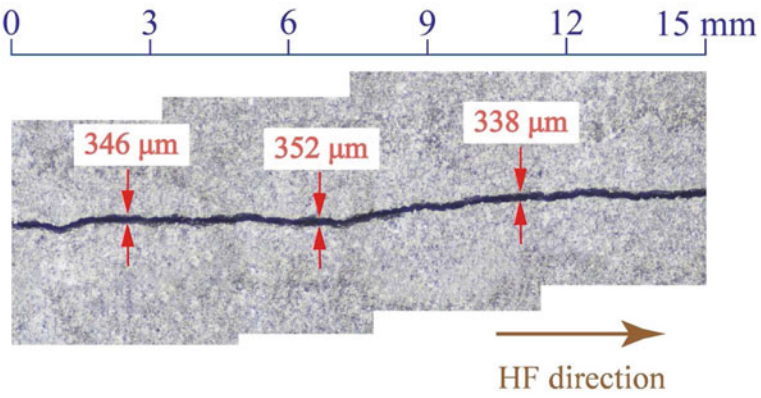

(b) Q_{inj}=30 mL/min，Sample CI-90-30 (corresponding to details in R_2 in Fig. 3.16 (e))

Fig. 4.17 Local growth path and width evolution of hydraulic fractures under different injection rates

rate range (≤12 mL/min), the injection rate has a significant effect on the standard deviation of section elevation. On the contrary, when the injection rate is greater than 12 mL/min, the disturbance effect of the injection rate on the fracture roughness is weakened. In general, SD decreased with the increase in injection rate, but the decrease of SD decreased gradually. When the injection rate exceeds the critical threshold (approximately 12 mL/min), the standard deviation of the fracture surface elevation tends to be constant.

To further quantify and characterize the relationship between the injection rate and the roughness morphology, the three-dimensional average inclination angle and

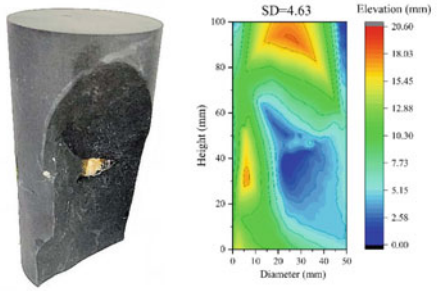

(a) Q_{inj}=3 mL/min，Sample CI-90-3

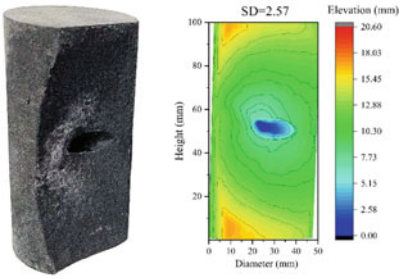

(d) Q_{inj}=18 mL/min，Sample CI-90-18

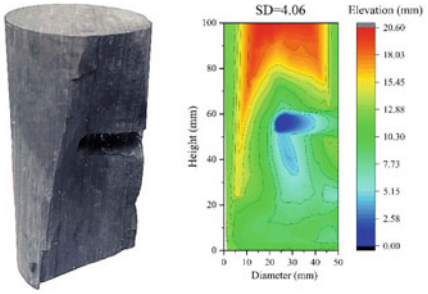

(b) Q_{inj}=6 mL/min, Sample CI-90-6

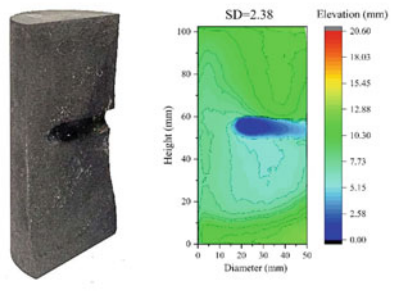

(e) Q_{inj}=30 mL/min，Sample CI-90-30

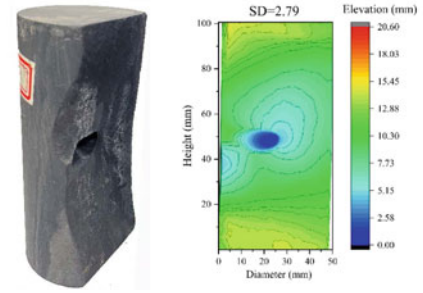

(c) Q_{inj}=12 mL/min, Sample CI-90-12

Fig. 4.18 Contour maps of vertical hydraulic fractures in shale samples under different injection rates

roughness coefficient of the fracture surface under different injection rates are calculated based on Eqs. (4.3) and (4.4). The results are summarized in Fig. 4.19. It should be noted that for sample CI-90-18 (Q_{inj} = 18 mL/min), the evolution trend of its three-dimensional average inclination angle and surface roughness coefficient presents completely opposite laws compared with its adjacent injection rate conditions. This phenomenon can be attributed to the difference in three-dimensional morphology of fracture surface caused by the heterogeneity of individual samples.

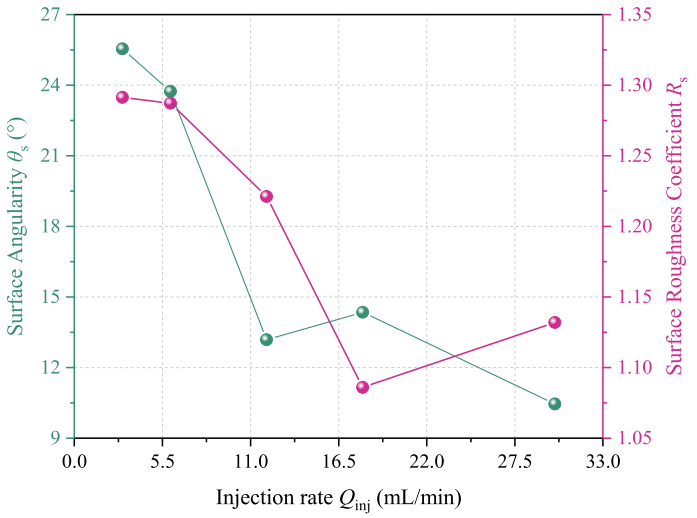

Fig. 4.19 Evolution of mean three-dimensional angle and roughness coefficient of hydraulic fracture surfaces under different injection rates

But overall, the three-dimensional average inclination and roughness coefficient of the fracture surface decreases with the injection rate, which further confirms the negative correlation and nonlinear correlation characteristics of the injection rate effect on the fracture surface morphology.

References

1. Zhuang L, Zang A (2021) Laboratory hydraulic fracturing experiments on crystalline rock for geothermal purposes[J]. Earth Sci Rev 1:103580
2. Lu GY, Gordeliy E, Prioul R, et al (2020) Time-dependent hydraulic fracture initiation [J]. J Geophys Res-Solid Earth 125(3)
3. Fallahzadeh SH, Shadizadeh SR, Pourafshary P (2010) Dealing with the challenges of hydraulic fracture initiation in deviated-cased perforated boreholes; proceedings of the Trinidad and Tobago energy resources conference, F, [C]. SPE-132797-MS
4. Wei M, Dai F, Ji Y, Wu W (2021) Effect of fluid pressure gradient on the factor of safety in rock stability analysis. Eng Geol. 294. https://doi.org/10.1016/j.enggeo.2021.106346
5. Lin C, He J, Li X, Wan X, Zheng B (2017) An experimental investigation into the effects of the anisotropy of shale on hydraulic fracture propagation. Rock Mech Rock Eng 50(3):543–554. https://doi.org/10.1007/s00603-016-1136-4
6. Jiang Z, Li Q, Hu Q, Liang Y, Xu Y, Liu L, Wu X, Li X, Wang X, Hu L, Ling F (2020) Acoustic emission characteristics in hydraulic fracturing of stratified rocks: a laboratory study. Powder Technol 371:267–276. https://doi.org/10.1016/j.powtec.2020.05.050
7. Baddari K, Frolov AD, Tourtchine V, Rahmoune F (2011) An integrated study of the dynamics of electromagnetic and acoustic regimes during failure of complex macrosystems using rock blocks. Rock Mech Rock Eng 44(3):269–280. https://doi.org/10.1007/s00603-010-0130-5

8. Hu X, Su G, Chen G, Mei S, Feng X, Mei G, Huang X (2019) Experiment on rock burst process of borehole and its acoustic emission characteristics. Rock Mech Rock Eng 52(3):783–802. https://doi.org/10.1007/s00603-018-1613-z
9. Li LR, Deng JH, Zheng L, Liu JF (2017) Dominant frequency characteristics of acoustic emissions in white marble during direct tensile tests. Rock Mech Rock Eng 50(5):1337–1346. https://doi.org/10.1007/s00603-016-1162-2
10. Jian-po L, Chang-yin Z, Ying-tao S, Ren W, Gang L, Shi-da X (2020) Temporal-spatial evolution of acoustic emission during progressive fracture processes around tunnel triggered by blast-induced disturbances under uniaxial and biaxial compression. Tunn Undergr Sp Technol. 96. https://doi.org/10.1016/j.tust.2019.103229
11. Wang C, Cao C, Liu Y, Li C, Li G, Lu H (2021) Experimental investigation on synergetic prediction of rock burst using the dominant-frequency entropy of acoustic emission. Nat Hazards 108(3):3253–3270 https://doi.org/10.1007/s11069-021-04822-6
12. Zang A, Wagner FC, Stanchits S, Dresen G, Andresen R, Haidekker MA (1998) Source analysis of acoustic emissions in Aue granite cores under symmetric and asymmetric compressive loads. Geophys J Int 135(3):1113–1130. https://doi.org/10.1046/j.1365-246X.1998.00706.x
13. Zhang ZH, Deng JH, Zhu JB, Li LR (2018) An experimental investigation of the failure mechanisms of jointed and intact marble under compression based on quantitative analysis of acoustic emission waveforms. Rock Mech Rock Eng 51(7):2299–2307. https://doi.org/10.1007/s00603-018-1484-3
14. Wang YS, Deng JH, Li LR, Zhang ZH (2019) Micro-failure analysis of direct and flat loading Brazilian tensile tests. Rock Mech Rock Eng 52(2). https://doi.org/10.1007/s00603-019-01877-7
15. Lei R, Zhang Z, Berto F, Ranjith PG, Liu L (2020) Cracking process and acoustic emission characteristics of sandstone with two parallel filled-flaws under biaxial compression. Eng Fract Mech. https://doi.org/10.1016/j.engfracmech.2020.107253
16. Ishida T, Aoyagi K, Niwa T, Chen Y, Murata S, Chen Q, Nakayama Y (2012) Acoustic emission monitoring of hydraulic fracturing laboratory experiment with supercritical and liquid CO_2. Geophys Res Lett https://doi.org/10.1029/2012GL052788
17. Hou P, Gao F, Gao Y, Yang Y, Cai C (2018) Changes in breakdown pressure and fracture morphology of sandstone induced by nitrogen gas fracturing with different pore pressure distributions. Int J Rock Mech Min Sci. https://doi.org/10.1016/j.ijrmms.2018.06.006
18. Rose W, Bruce WA (1949) Evaluation of capillary character in petroleum reservoir rock. J Pet Technol. https://doi.org/10.2118/949127-g
19. Guo P, Li X, Li S, Yang W, Wu Y, Li G (2021) Quantitative analysis of anisotropy effect on hydrofracturing efficiency and process in shale using x-ray computed tomography and acoustic emission. Rock Mech Rock Eng. https://doi.org/10.1007/s00603-021-02589-7
20. Ishibashi T, Fang Y, Elsworth D, Watanabe N, Asanuma H (2020) Hydromechanical properties of 3D printed fractures with controlled surface roughness: insights into shear-permeability coupling processes. Int J Rock Mech Min Sci. https://doi.org/10.1016/j.ijrmms.2020.104271
21. Belem T, Homand-Etienne F, Souley M (2000) Quantitative parameters for rock joint surface roughness. Rock Mech Rock Eng. https://doi.org/10.1007/s006030070001
22. El-Soudani SM (1978) Profilometric analysis of fractures. Metallography. https://doi.org/10.1016/0026-0800(78)90045-9
23. Chitrala Y, Moreno C, Sondergeld C, Rai C (2011) Microseismic and microscopic analysis of laboratory induced hydraulic fractures. In: Society of petroleum engineers—Canadian unconventional resources conference 2011, CURC 2011
24. Zeng Z, Roegiers JC (2002) Experimental observation of injection rate influence on the hydraulic fracturing behavior of a tight gas sandstone. In: Proceedings of the SPE/ISRM rock mechanics in petroleum engineering conference
25. Shao CY, Pan PZ, Zhao DC, Yao TB, Miao ST (2020) Effect of pumping rate on hydraulic fracturing breakdown pressure and pressurization rate. Rock Soil Mech 41(07):2411–2421+2484
26. Zhuang L, Kim KY, Jung SG, Diaz M, Min KB (2019) Effect of water infiltration, injection rate and anisotropy on hydraulic fracturing behavior of granite. Rock Mech Rock Eng. https://doi.org/10.1007/s00603-018-1431-3

27. Haimson BC (1968) Hydraulic fracturing in porous and nonporous rock and its potential for determining in-situ stresses at great depth. Doctoral thesis, University of Minnesota
28. Zoback MD, Rummel F, Jung R, Raleigh CB (1977) Laboratory hydraulic fracturing experiments in intact and pre-fractured rock. Int J Rock Mech Min Sci. https://doi.org/10.1016/0148-9062(77)90196-6
29. Solberg P, Lockner D, Byerlee J (1977) Shear and tension hydraulic fractures in low permeability rocks. Pure Appl Geophys PAGEOPH. https://doi.org/10.1007/BF01637103
30. Chitrala Y, Sondergeld C, Rai C (2012) Microseismic studies of hydraulic fracture evolution at different pumping rates. In: Society of petroleum engineers—SPE Americas unconventional resources conference 2012
31. AlTammar MJ, Sharma MM (2019) Effect of borehole pressurization scheme on breakdown pressure. Rock Mech Rock Eng. https://doi.org/10.1007/s00603-018-1731-7
32. Detournay E, Cheng A (1992) Influence of pressurization rate on the magnitude of the breakdown pressure. In: 33rd U.S. symposium on rock mechanics, USRMS 1992
33. Duan K, Kwok CY, Wu W, Jing L (2018) DEM modeling of hydraulic fracturing in permeable rock: influence of viscosity, injection rate and in situ states. Acta Geotech. https://doi.org/10.1007/s11440-018-0627-8
34. Li N, Zhang S, Zou Y, Ma X, Zhang Z, Li S, Chen M, Sun Y (2018) Acoustic emission response of laboratory hydraulic fracturing in layered shale. Rock Mech Rock Eng. https://doi.org/10.1007/s00603-018-1547-5
35. Zou YS, Zhang SC, Zhou T, Zhou X, Guo TK (2016) Experimental investigation into hydraulic fracture network propagation in gas shales using CT scanning technology. Rock Mech Rock Eng. https://doi.org/10.1007/s00603-015-0720-3
36. Zhao Z, Zhao Y, Jiang Z, Guo J, Zhang R (2021) Investigation of fracture intersection behaviors in three-dimensional space based on CT scanning experiments. Rock Mech Rock Eng. https://doi.org/10.1007/s00603-021-02587-9